

UNCLASSIFIED

AD NUMBER
ADB016942
NEW LIMITATION CHANGE
TO Approved for public release, distribution unlimited
FROM Distribution authorized to U.S. Gov't. agencies only; Test and evaluation; Feb 1977. Other requests shall be referred to Space and Missile Systems Organization, Attn: RSSR, P.O. Box 92960, Worldway Postal Center, Los Angeles, CA 90009.
AUTHORITY
USAF Ltr, dtd 12 Apr 1978

THIS PAGE IS UNCLASSIFIED

THIS REPORT HAS BEEN DELIMITED
AND CLEARED FOR PUBLIC RELEASE
UNDER DOD DIRECTIVE 5200.20 AND
NO RESTRICTIONS ARE IMPOSED UPON
ITS USE AND DISCLOSURE.

DISTRIBUTION STATEMENT A

APPROVED FOR PUBLIC RELEASE;
DISTRIBUTION UNLIMITED.

2

FG



**HEAT-TRANSFER AND STATIC STABILITY TESTS OF A 7.5-DEG
BLUNT CONE WITH ROUGHNESS ELEMENTS AND SONIC
JETS TO PROMOTE BOUNDARY-LAYER
TRANSITION AT MACH NUMBER 10**

VON KARMAN GAS DYNAMICS FACILITY
ARNOLD ENGINEERING DEVELOPMENT CENTER
AIR FORCE SYSTEMS COMMAND
ARNOLD AIR FORCE STATION, TENNESSEE 37389

February 1977

Final Report for Period 1 April — 31 July 1976

Distribution limited to U.S. Government agencies only; this report contains information on test and evaluation of military hardware; February 1977; other requests for this document must be referred to Space and Missile Systems Organization (SAMSO/RSSR), P.O. Box 92960, Worldway Postal Center, Los Angeles, CA 90009.

D D C
RECEIVED
MAR 14 1977

Prepared for

SPACE AND MISSILE SYSTEMS ORGANIZATION (RSSR)
P. O. BOX 92960, WORLDWAY POSTAL CENTER
LOS ANGELES, CALIFORNIA 90009

ADB016942

NO. 1
DOC FILE COPY

UNCLASSIFIED

REPORT DOCUMENTATION PAGE		READ INSTRUCTIONS BEFORE COMPLETING FORM
1. REPORT NUMBER AEDC-TR-76-157	2. GOVT ACCESSION NO.	3. RECIPIENT'S CATALOG NUMBER
4. TITLE (and Subtitle) HEAT-TRANSFER AND STATIC STABILITY TESTS OF A 7.5-DEG BLUNT CONE WITH ROUGHNESS ELEMENTS AND SONIC JETS TO PROMOTE BOUNDARY-LAYER TRANSITION AT MACH NUMBER 10		5. DATE OF REPORT & PERIOD COVERED Final Report, 1 April - 31 July 1976
6. AUTHOR(s) D. B. Carver, J. T. Best, Jr., and W. R. Martindale, ARO, Inc.		7. PERFORMING ORG. REPORT NUMBER
8. PERFORMING ORGANIZATION NAME AND ADDRESS Arnold Engineering Development Center (XO) Air Force Systems Command Arnold Air Force Station, TN 37389		9. CONTRACT OR GRANT NUMBER(s)
10. CONTROLLING OFFICE NAME AND ADDRESS Space and Missile Systems Organization (RSSR), P.O. Box 92960, Worldway Postal Center, Los Angeles, CA 90009		11. PROGRAM ELEMENT, PROJECT, TASK AREA & WORK UNIT NUMBERS Program Element 63311F System 627A Task 01
12. MONITORING AGENCY NAME & ADDRESS (if different from Controlling Office)		13. REPORT DATE February 1977
14. DISTRIBUTION STATEMENT (of this Report) Distribution limited to U.S. Government agencies only; this report contains information on test and evaluation of military hardware; February 1977; other requests for this document must be referred to Space and Missile Systems Organization (SAMSO/RSSR), P. O. Box 92960, Worldway Postal Center, Los Angeles, CA 90009.		15. NUMBER OF PAGES 68
16. DISTRIBUTION STATEMENT (of the abstract entered in Block 20, if different from Report)		17. SECURITY CLASS (of this report) UNCLASSIFIED
18. SUPPLEMENTARY NOTES Available in DDC.		19. DECLASSIFICATION DOWNGRADING SCHEDULE N/A
20. KEY WORDS (Continue on reverse side if necessary and identify by block number) reentry vehicles boundary-layer control conical bodies blunt cones models boundary-layer transition wind tunnel tests		
21. ABSTRACT (Continue on reverse side if necessary and identify by block number) Aerothermodynamic transition tests were conducted on a 7.5-deg half-angle, blunt cone model to evaluate variations of trip design in promoting boundary-layer transition on a reentry vehicle. Heat-transfer data were obtained using square-shaped roughness elements and sonic jets as boundary-layer trips to determine the effects of 1) trip height, 2) trip spacing, 3) axial trip location, 4) number of rows of trips, 5) staggered trips, and 6) Reynolds.		

DD FORM 1473 EDITION OF 1 NOV 65 IS OBSOLETE

UNCLASSIFIED

0112550

UNCLASSIFIED

20. ABSTRACT (Continued)

number on heat-transfer distributions. Static stability tests were conducted in conjunction with a few selected trip configurations to determine the influence of the boundary-layer trips on the model static stability and axial-force characteristics. The tests were performed at Mach number 10 for angle-of-attack ranges from 0 to 2 deg (heat-transfer data) and from -7.5 to 7.5 deg (static stability data). Free-stream Reynolds number, based on total model length, was varied from 1.5 to 6.2 million. Selected heat-transfer and static stability data are presented to illustrate the effects of configuration variables and Reynolds number.

APR 1
Arnold AFB Tenn

UNCLASSIFIED

PREFACE

The work reported herein was conducted by the Arnold Engineering Development Center (AEDC), Air Force Systems Command (AFSC), at the request of the Space and Missile Systems Organization (SAMSO/RSSR), for the AVCO Systems Division, Wilmington, Massachusetts, under Program Element 63311F. The results of the tests were obtained by ARO, Inc., AEDC Division (a Sverdrup Corporation Company), operating contractor for the AEDC, AFSC, Arnold Air Force Station, Tennessee, under ARO Project Number V41C-H3A. The authors of this report were D. B. Carver, J. T. Best, Jr., and W. R. Martindale, ARO, Inc. Data reduction was completed on August 16, 1976, and the manuscript (ARO Control No. ARO-VKF-TR-7(-124) was submitted for publication on October 20, 1976.

The authors wish to express their gratitude to Mr. P. A. Jalbert, ARO, Inc., for his assistance during the tests and to Dr. A. W. Mayne, Jr., and Mrs. Betty Majors, ARO, Inc., for performing the theoretical computations.

CONTENTS

	<u>Page</u>
1.0 INTRODUCTION	7
2.0 APPARATUS	
2.1 Wind Tunnel	8
2.2 Model	8
2.3 Instrumentation	10
3.0 PROCEDURES	
3.1 Test Conditions	14
3.2 Heat-Transfer Tests	15
3.3 Force Tests	16
3.4 Data Reduction	16
3.5 Data Uncertainty	18
4.0 RESULTS AND DISCUSSION	
4.1 Heat-Transfer Tests	21
4.2 Force Tests	25
5.0 CONCLUDING REMARKS	27
REFERENCES	28

ILLUSTRATIONS

Figure

1. Tunnel C	31
2. Photograph of Model in Tunnel C Tank	32
3. Trip Section Photographs	33
4. Model Details	38
5. Chromel [®] -Constantan Coaxial Surface Thermocouple Gage, 10X Scale	43
6. Typical Shadowgraphs, $Re_{\infty, L} = 6.2 \times 10^6$, $\alpha = 0$	44
7. Comparison of Smooth Model Heat-Transfer Data to Theory at $\alpha = 0$	45
8. Effect of Angle of Attack on the Smooth Model Heat-Transfer Distribution	46

FigurePage

9. Effect of Angle of Attack on a Turbulent Heat-Transfer Distribution (Configuration 1020-0303-1515), $Re_{\infty,L} = 6.2 \times 10^6$	47
10. Effect of Trip Height and Number of Rows on Transition at $Re_{\infty,L} = 6.2 \times 10^6$, Narrow-Spaced Passive Trips at $S/R_n = 4.5$	48
11. Typical Oil Flow Photographs, $Re_{\infty,L} = 6.2 \times 10^6$	49
12. Effect of Circumferential Trip Spacing on the Heat-Transfer Distribution Uniformity for Passive Trips, One Row at $S/R_n = 4.5$, $k = 0.100$ in., $Re_{\infty,L} = 6.2 \times 10^6$	51
13. Effect of Axial Trip Location on Transition Length, Three Rows of Narrow-Spaced Passive Trips, $k = 0.100$ in., $Re_{\infty,L} = 6.2 \times 10^6$	52
14. Effect of Reynolds Number on Transition, Narrow-Spaced Passive Trips at $S/R_n = 4.5$	53
15. Effect of Trip Height and Number of Rows on Transition at $Re_{\infty,L} = 6.2 \times 10^6$, Narrow-Spaced Active Trips at $S/R_n = 4.5$	54
16. Effect of Circumferential Orifice Spacing on the Heat-Transfer Distribution Uniformity for Active Trips, One Row at $S/R_n = 4.5$, $k = 0.033$ in. ($p_c = 1.5$ psia), $Re_{\infty,L} = 6.2 \times 10^6$	55
17. Effect of Various Passive Trips on the Longitudinal Stability and Axial-Force Characteristics, $Re_{\infty,L} = 6.2 \times 10^6$	56
18. Effect of Active Trip Configurations on the Longitudinal Stability and Axial-Force Characteristics, $Re_{\infty,L} = 6.2 \times 10^6$	57
19. Effect of Reynolds Number on Axial Force for a Passive Configuration (1020-0505-1010) at $\alpha = 0$	58
20. Effect of Mass Injection on Axial Force at $\alpha = 0$ for Various Reynolds Numbers (Configuration 3120-0303-0000)	59

TABLES

	<u>Page</u>
1. Passive Trip Dimensions	60
2. Heat-Transfer Test Summary	61
3. Force Test Summary	63
 NOMENCLATURE	 64

1.0 INTRODUCTION

During reentry, some vehicles may exhibit an angle-of-attack divergence in the altitude regime where the boundary layer on the body is transitional. Such behavior often results in transition-induced dispersion and can be detrimental to the system performance of ballistic and maneuvering reentry vehicles. The tests described herein were performed to obtain data which will assist in the design of reliable boundary-layer-tripping configurations for the control of transition-induced dispersion by forcing the boundary layer to become and remain turbulent early in the reentry. The model selected for this investigation was a 7.5-deg half-angle cone with a bluntness ratio, R_n/R_b , of 0.167. Two basic tripping methods were used: (1) passive (roughness) and (2) active (mass injection). The passive trips were primarily square-shaped protuberances of a specified height. The active trips consisted of sonic jets of gaseous nitrogen ejected from small orifices in the model surface.

An initial screening investigation was made to obtain heat-transfer data at Reynolds numbers corresponding to those for flight altitudes down to 125,000 ft. The state of the boundary layer was inferred from these heat-transfer distributions. This investigation covered the effects on the heat-transfer distributions of (1) trip height, (2) trip spacing, (3) trip location, (4) number of rows of trips, (5) staggered trips, and (6) Reynolds number. The angle-of-attack range was from 0 to 2 deg at zero sideslip for all heat-transfer tests.

Static-force and moment data were also obtained for models with selected trip configurations (passive and active) to evaluate the effects of transition and trip design on the model static stability and drag. The angle-of-attack range for the force test was from -7.5 to 7.5 deg.

The tests were conducted in the AEDC von Kármán Gas Dynamics Facility (VKF) Hypersonic Wind Tunnel (C) at Mach number 10. Nominal test Reynolds numbers, based on total model length, were from 1.5 to 6.2 million. Additional heat-transfer and force tests on the same vehicle geometry have been conducted in the AEDC Hypervelocity Wind Tunnel (F). The latter results are to be documented in a forthcoming report.

2.0 APPARATUS

2.1 WIND TUNNEL

Tunnel C (Fig. 1) is a closed-circuit, hypersonic wind tunnel with a Mach number 10 axisymmetric contoured nozzle and a 50-in.-diam test section. The tunnel can be operated continuously over a range of pressure levels from 200 to 2,000 psia with air supplied by the VKF main compressor plant. Stagnation temperatures sufficient to avoid air liquefaction in the test section (up to 1,900°R) are obtained through the use of a natural gas-fired combustion heater in series with an electric resistance heater. The entire tunnel (throat, nozzle, test section, and diffuser) is cooled by integral, external water jackets. The tunnel is equipped with a model injection system which allows removal of the model from the test section while the tunnel remains in operation. A more complete description of the tunnel is presented in Ref. 1.

2.2 MODEL

Basic model geometry consisted of a 7.5-deg half-angle sphere cone with a bluntness ratio of 0.167, which corresponds to the geometry of the Technology Development Vehicle (TDV). The model used in this test program had a base diameter of 10.0 in., whereas the flight vehicle has a base diameter of 24.0 in.; hence the model was a 0.417-scale model of the flight vehicle.

Primarily a heat-transfer/pressure model, the model was designed and fabricated by AVCO Systems Corporation. The aft section was common to all configurations, and there were three different midsections: "trip," "short-blow," and "long-blow." A photograph of an assembled model is presented in Fig. 2, and photographs of the various trip sections are shown in Fig. 3. Model sketches are presented in Fig. 4.

The midsection trip, together with various trip and spacer sections, was used to assemble the various passive configurations. Details of the midsection trip and the trip sections are shown in Fig. 4b and c, respectively. The heat-transfer instrumentation on the trip sections was enhanced by a quick-disconnect (miniature plugs) system which permitted installation of gages on the trip sections and minimized the time required to make model changes.

The midsection short-blow had two interchangeable cone sections; one of the sections had orifices with 40-deg spacing, and the other had 20-deg spacing. The first row of orifices was located at $S/R_n = 4.5$. Orifice locations are shown in Fig. 4d.

The midsection long-blow (Fig. 4e) also had two interchangeable sections. One section had three rows of orifices with 15-deg spacing, with the first row at $S/R_n = 8.5$. The other section had ten rows of orifices with 20-deg spacing, with the first row at $S/R_n = 4.5$. All orifices were 0.0215 in. in diameter.

Straight pins (0.020-in. diam) were used to plug some of the orifices to make various configurations (spacing, number of rows, staggered orifices). A quick-setting silicone rubber was used to seal the plugged orifices.

All parts of the model were machined from stainless steel, with the exception of an extra nosetip which was made from copper to serve as a heat sink for the force tests.

Two passive trip geometries were tested: (1) rectangular trips and (2) a triangular or saw-tooth geometry trip, which was a simulated ablated shape of the rectangular trips. The rectangular trips were 0.20 in. square and protruded above the model surface by a height, k . The rectangular trips were chosen because of their simplicity for machining directly on the flight vehicle surface. The saw-tooth trips (Fig. 3e) were obtained by machining the rectangular trips to form a triangular shape, from both a planform view and the side view. All trips were designed to have a nominal trip spacing of either 0.4 in. (narrow spacing) or 0.8 in. (wide spacing) in the first row. Presented in Table 1 is a complete listing of the critical dimensions for all the passive trip configurations tested.

2.3 INSTRUMENTATION

2.3.1 General

Tunnel C stilling chamber pressure is measured with a 500- or 2,500-psid transducer referenced to a near vacuum. Based on periodic comparisons with secondary standards, the uncertainty (a bandwidth which includes 95 percent of residuals) of the transducers is estimated to be within ± 0.1 percent of reading or ± 0.25 psi, whichever is greater, for the 500-psid range and ± 0.1 percent of reading or ± 1.25 psi, whichever is greater, for the 2,500-psid range. Stilling chamber temperature measurements are made with Chromel[®]-Alumel[®] thermocouples which have an uncertainty of $\pm(1.5^{\circ}\text{F} + 0.375 \text{ percent of reading})$ based on repeat calibrations.

2.3.2 Heat-Transfer Tests

Coaxial surface thermocouple gages were used to measure the surface heating-rate distributions. This type gage was chosen because of its capability to function in the test environments of both continuous tunnels

and impulse tunnels. This capability made it possible to use the same heat-transfer gages for the tests in Tunnel F and Tunnel C. The primary limitation of this gage is the short allowable time of exposure to a constant heat flux: before the assumption that the gage will behave as a semi-infinite solid becomes invalid.

The coaxial gage (see Fig. 5) consists of an electrically insulated Chromel center conductor enclosed in a cylindrical constantan jacket. After assembly and installation in the model, the gage materials are blended together with a jeweler's file. This results in thermal and electrical contact between the two materials in a thin layer at the surface of the gage; that is, a surface thermocouple is formed. A second result of filing the gage surface is the opportunity for "perfect" contouring of the gage to the model surface. This fact was important in the selection of coaxial gages since a smooth model is essential in transition studies. A total of 192 individually calibrated gages was supplied and installed by the VKF, with 97 gages the maximum for any configuration.

Fluctuating model surface pressure measurements were made at a maximum of eight locations using miniature dynamic pressure transducers manufactured by Kulite Semiconductor Products, Inc. Also, a "flight transducer package," consisting of three dynamic pressure transducers (Bolt, Baranek and Newman, BBN model 376) and two accelerometers (BBN model 508) was located near the base of the model. Instrumentation of this type is to be used on the flight vehicle and was included on this test to evaluate its performance in detecting boundary-layer transition. Each of the flight pressure transducers had a different installation arrangement: flush, slightly recessed, and ported. Data from the dynamic pressure transducers were recorded on analog tape and transmitted to AVCO Systems for analysis.

The model plenum chamber pressure, p_c , was measured using a 200-psid

transducer referenced to a near vacuum with two pairs of full-scale calibrated ranges (20 to 200 and 2 to 50 psia). The first pair was used for initial test data, and the second pair was used for additional test data after it was determined that the higher pressure range was not required. Estimated precision of this transducer is ± 1.0 percent of full scale of the range being used.

A Chromel-Alumel thermocouple was located inside the model plenum chamber to measure the gas temperature with an estimated precision of ± 0.75 percent based on the thermocouple wire manufacturer's specifications.

Measurement of the mass flow rate of the nitrogen gas being supplied to the model chamber (for active configurations) was made using the VKF "Low Mass-Flow System." The system uses hot-film flowmeters and can measure flow rates from 3.6×10^{-7} to 4.8×10^{-2} lbm/sec of gaseous nitrogen. However, the flowmeter used for the heat-transfer tests and the required operational procedures limited the minimum measurement rate to 2.0×10^{-4} lbm/sec. Estimated precision of the mass flow rates using the hot-film flowmeter ($\dot{m} > 2.0 \times 10^{-4}$ lbm/sec) was ± 10.0 percent. Bench tests were performed subsequent to test completion to evaluate the model orifice discharge coefficients. These coefficients, together with the measured plenum chamber pressure and temperature, were used to calculate the mass flow rates when the measured value was less than 2.0×10^{-4} lbm/sec. Uncertainty of the flow rates computed in this manner is estimated to be ± 15.0 percent ($\dot{m} \leq 2.0 \times 10^{-4}$ lbm/sec).

2.3.3 Force Tests

Model forces and moments were measured with a six-component, moment type, strain-gage balance supplied and calibrated by VKF. Prior to the test, static loads in each plane and combined static loads were applied to the balance to simulate the range of loads and center-of-pressure locations anticipated during the test. The following uncer-

tainties represent the bands of 95 percent of the measured residuals, based on differences between the applied loads and the corresponding values calculated from the balance calibration equations included in the final data reduction. The range of check loads applied and the measurement uncertainties follow.

<u>Component</u>	<u>Balance Design Loads</u>	<u>Calibration Load Range</u>	<u>Range of Check Loads</u>	<u>Measurement Uncertainty</u>
Normal Force, lb	± 200	± 150	±100	±0.2
Pitching Moment, in.-lb	±1,320	±1,050	±400	±1.3
Axial Force, lb	50	50	30	±0.23

*About balance forward moment bridge.

The transfer distance from the balance forward-moment bridge to the model moment reference location was 16.24 in. along the longitudinal axis and was measured with an estimated precision of ±0.01 in.

Model base pressures (see Fig. 4a for locations) were measured with either the standard base pressure system or a fast response transducer, depending upon the mode of taking data. When in the pitch-pause mode of data taking (see Section 3.3), the model base pressures and model cavity pressure were measured with the standard base pressure system, which is comprised of 1-psid transducers referenced to a near vacuum. The uncertainty of these transducers is ±0.3 percent of reading or ±0.0005 psi, whichever is greater. For the continuous sweep mode of operation, the model base pressure was measured on a 5-psid fast response transducer referenced to a near vacuum which was calibrated for a full-scale reading of 0.05 psi. The uncertainty of this transducer is ±1.0 percent of reading, based on comparisons with the standard base pressure system.

As a result of the initial heat-transfer tests, an improved system was used to measure the model plenum chamber pressure and the mass flow rates for the force tests. The model plenum chamber pressure was measured with a 15-psid transducer referenced to a near vacuum. The uncertainty of this transducer is ± 0.2 percent of reading or ± 0.01 psi, whichever is greater. Mass flow rates were measured using the same system (see Section 2.3.2) as for the heat-transfer tests; however, a smaller flowmeter and revised procedures improved the measurement precision to approximately ± 5.0 percent for all data.

The model wall temperature just aft of the trip sections was measured with a coaxial surface thermocouple to monitor the model temperature variation during the test and thereby avoid large temperature rises during a run.

3.0 PROCEDURES

3.1 TEST CONDITIONS

All tests were performed at a nominal Mach number of 10 over a Reynolds number range, based on total model length, from 1.5 to 6.2 million. A summary of the nominal test conditions follows. A complete test summary for the heat-transfer and force data obtained is presented in Tables 2 and 3, respectively.

TEST CONDITIONS

P_o , psia	T_o , °R	M_∞	q_∞ , psia	P_∞ , psia	St_{ref}	ρ_∞ , lbm/ft ³	u_∞ , ft/sec	$Re_{\infty,L} \times 10^6$
450	1,900	10.02	0.70	0.0100	0.0317	0.000285	4,765	1.51
650		10.05	1.00	0.0141	0.0266	0.000406	4,770	2.15
850		10.11	1.28	0.0178	0.0235	0.000519	4,770	2.79
1,050		10.11	1.59	0.0222	0.0211	0.000643	4,775	3.46
1,250		10.14	1.87	0.0260	0.0194	0.000758	4,775	4.10
1,450		10.14	2.18	0.0303	0.0180	0.000885	4,780	4.77
1,650		10.14	2.49	0.0346	0.0168	0.00101	4,780	5.46
1,900		10.17	2.85	0.0393	0.0158	0.00115	4,780	6.24

All free-stream parameters are computed assuming a real gas, isentropic expansion from the tunnel stilling chamber and utilizing the measured pressure and temperature at the stilling chamber and the calibrated Mach number at the test section.

When sonic jets are used as boundary-layer trips, a computed trip height is sometimes used (see Ref. 2, for example) to correlate the jet-trip effectiveness. The active trip height, k' , was computed using the sonic jet penetration height as the distance from the model surface to the normal shock wave in the jet plume (see Fig. 4d), as described in Ref. 3, with the AVCO equations (shown in the Nomenclature). Dry nitrogen was used as the injectant gas, and the measured values of plenum chamber pressure, p_c , and mass injection rate, \dot{m} , are presented to document the test conditions with trip height, k' , listed in the active trip data figures.

3.2 HEAT-TRANSFER TESTS

Prior to each test run the model configuration was prepared, the test conditions were established, and for active configurations the plenum chamber pressure was preset. The model was injected into the tunnel flow for a test run and then retracted into the test section tank, where it was cooled. Cooling was accomplished by blowing high pressure air over the model. The model was in the tunnel flow (from injection to retraction) approximately 8 sec. During this time the model wall temperature was nominally 540 to 560°K. The model was inspected periodically to assure that the desired angle of attack was precise within ± 0.1 deg. Shadowgraph photographs were taken during nearly all test runs to monitor the flow conditions. Selected shadowgraphs are presented in Fig. 6.

Oil flow photographs of the model were taken from the "nonoperating" side of the tunnel during a few runs (see Table 2). All model instrumentation was located on the "operating" side ($\theta_g = 0$ to 180 deg); therefore, the heat-transfer data were unaffected by the oil flow.

The gage (thermocouple) outputs, together with the test conditions, were recorded on magnetic tape using a Beckman 210 analog-to-digital converter. Each thermocouple output was recorded 17 times per second from the start of the model injection cycle until 3 sec after the model reached tunnel centerline.

3.3 FORCE TESTS

The force and moment data were obtained by two modes of operation: pitch-pause and continuous sweep. In the pitch-pause mode of operation, the angle of attack was set and 32 samples of data were taken and averaged to find the values at that angle. Data were also taken in the continuous sweep mode at the rate of 144 samples per second while the angle of attack was continuously driven at the rate of approximately 1 deg per second. Every 32 samples were averaged, and then the two averaged values on either side of the required angle were interpolated to obtain the values at that angle. The continuous sweep mode was used for most of the data because it reduced the time the model was in the tunnel (and thus prevented model overheating and distortion).

The model was cooled with high pressure air prior to each test run to maintain a wall temperature ratio (T_w/T_o) of 0.28 to 0.39. Shadowgraph pictures were taken during the force tests at specific angles of attack.

3.4 DATA REDUCTION

3.4.1 Heat-Transfer

The coaxial gage provides measurement of the surface temperature of the gage-model composite, which is assumed to be a homogenous, one-dimensional, semi-infinite solid. However, the gages and the model wall are of finite thickness, and the semi-infinite solid assumption was valid for a maximum of about 2 sec after the model reached tunnel centerline. This time was

adequate for data acquisition, and the above assumptions were used to compute the heat flux at the model surface. The data were reduced using the numerical integration technique originally developed by Cook and Felderman (Ref. 4), which does not involve assumptions about the nature of the heating input. The Cook and Felderman expression for the surface heat flux has been reduced to

$$\dot{q}(t_n) = 2 \sqrt{\frac{(\rho c k)_g}{\pi}} \left(\sum_{i=1}^n \frac{\bar{T}_i - \bar{T}_{i-1}}{\sqrt{t_n - t_{i-1}} + \sqrt{t_n - t_i}} \right) \cdot \frac{Btu}{ft^2 \cdot sec}$$

where t = time from start of model injection cycle,
sec (at any time t_n , n samples of data
have been taken)

t_i = time corresponding to data sample
number i , sec

t_n = time at which the heat-transfer rate
 $\dot{q}(t_n)$ was calculated, sec

$(\rho c k)_g$ = Product of the gage density,
specific heat and conductivity,
 $Btu^2/ft^4 \cdot sec \cdot ^\circ R^2$

\bar{T} = Gage surface temperature at the
subscripted time minus the gage surface
temperature at start of injection cycle, $^\circ R$

All heat-transfer data were converted to Stanton numbers and nondimensionalized by the model nose stagnation Stanton number. The stagnation Stanton number (St_{ref}) was computed using Fay-Riddell theory (Ref. 5).

3.4.2 Aerodynamic Coefficients

Balance forces and moments were transferred to the model moment reference point at the nosetip and reduced to coefficients in the body-axis system. The coefficient reference length was the total model length (L), and reference area was the model base area (A_b).

The center-of-pressure location from the model nose, referenced to the model length (X_{cp}/L), was calculated using two methods. For all angles of attack except zero, X_{cp}/L was defined as C_m divided by C_{N_α} . For the continuous sweep mode data, the value of center-of-pressure at $\alpha = 0$ was determined from the ratio of the derivatives ($X_{cp}/L \equiv C_{m_\alpha}/C_{N_\alpha}$).

Forebody axial-force coefficients were obtained using the measured base axial-force coefficient, C_{A_b} , which was calculated using the average of the two base pressures and one cavity pressure when in the pitch-pause mode, or the base pressure from the fast response transducer when in the continuous sweep mode.

Since the basic model was a symmetrical configuration, trim effects in the continuous-sweep data were corrected for possible flow angularity, model misalignment, and free-stream nonuniformity effects (i.e., C_m induced without corresponding C_N). The result is that both normal force and pitching moment are corrected to be zero at $\alpha = 0$.

3.5 DATA UNCERTAINTY

An evaluation of the influence of random measurement errors is presented in this section to provide a measure of the uncertainty of the final test results. Although evaluation of the systematic measurement error (bias) is not included, it should be noted that the instrumentation precision values (given in Section 2.3) used in this evaluation represent a total uncertainty including both systematic and random (two-standard deviation bandwidth) error contributions.

3.5.1 Test Conditions

Uncertainties in the basic tunnel parameters p_o and T_o (see Section 2.3.1) and the two-standard deviation uncertainty in Mach number determined from test section flow calibrations were used to estimate uncertainties in the other free-stream properties, using the Taylor series method of error propagation.

Test Condition Uncertainty (\pm), percent									
p_o , psia	p_o	T_o	M_∞	q_∞	p_∞	St_{ref}	p_∞	u_∞	$Re_{\infty,L}$
450	0.1	0.4	1.0	4.7	6.7	5.3	4.8	0.2	2.9
650	0.2		1.0	4.7	6.6	5.3	4.8		2.9
850	0.15		0.8	3.7	5.3	4.3	3.8		2.3
1,050	0.12								
1,250	0.1								
1,450									
1,650									
1,900									

3.5.2 Heat-Transfer Data

Uncertainties in the calibrations of the coax gages are estimated to be ± 5.0 percent based on the calibration repeatability. An examination of the data showed the Stanton number ratio (St/St_{ref}) to repeat within ± 10 percent for data from the same configuration and test conditions.

3.5.3 Aerodynamic Coefficients

The balance and base pressure uncertainties listed in Section 2.3.3 were combined with uncertainties in the tunnel parameters, using the Taylor series method of error propagation, to estimate the uncertainty

of the aerodynamic coefficients, and these are presented below.

Measured Coefficient Uncertainty (\pm), percent

<u>p_o, psia</u>	<u>C_N</u>	<u>C_m</u>	<u>C_{A_t}</u>	<u>C_A</u>
650	5.7	5.6	6.1	7.2
850	3.8	3.8	4.2	4.9
1,050	3.8	3.7	4.1	4.8
1,450	3.7	3.7	3.9	4.8
1,900	3.7	3.7	3.8	4.6

The basic precision of the aerodynamic coefficients was also computed using only the balance and base pressure uncertainties listed in Section 2.3.3 along with the nominal test conditions, using the assumption that the free-stream flow nonuniformity is a bias type of uncertainty which is constant for all test runs. These values therefore represent the data repeatability expected and are especially useful for detailed discrimination purposes in parametric model studies.

Measured Coefficient Repeatability (\pm)

<u>p_o, psia</u>	<u>C_N</u>	<u>C_m</u>	<u>C_{A_t}</u>	<u>C_A</u>
650	0.0025	0.0005	0.0029	0.0034
850	0.0020	0.0004	0.0023	0.0026
1,050	0.0016	0.0003	0.0018	0.0021
1,450	0.0011	0.0002	0.0013	0.0016
1,900	0.0009	0.0002	0.0010	0.0012

The uncertainty in model angle of attack (α), as determined from tunnel sector calibrations and consideration of the possible errors in model deflection calculations, is estimated to be ± 0.1 deg.

4.0 RESULTS AND DISCUSSION

4.1 HEAT-TRANSFER TESTS

The fundamental objective of the test program was to obtain data which would make possible the design of reliable tripping configurations for the control of transition-induced dispersion during flight vehicle reentry. Therefore, the majority of the heat-transfer tests were devoted to configuration variables at the maximum Reynolds number ($Re_{\infty,L} = 6.2 \times 10^6$) and $\alpha = 0$. Additional data were taken on selected configurations to observe the effects of Reynolds number and small angles of attack. Representative data have been selected from the test results for presentation and discussion. The theoretical heat-transfer rate distributions shown in all figures were obtained from calculations using the method of Patankar and Spaulding (Ref. 6) as modified by Mayne and Dyer (Ref. 7). This method uses an axisymmetric body at zero incidence to define the geometry. The required inviscid computational data were obtained using the method of Ref. 8.

Heat-transfer-rate distributions on the basic smooth model at $\alpha = 0$ are shown in Fig. 7 with a theoretical solution for comparison. Instrumentation consistency is illustrated by the good agreement between distributions for each of the constant θ_g rays, which should be the case for this symmetric model at zero incidence. Additional data from the active trip configuration but with no blowing show the data to be repeatable and are typical of the repeatability obtained during the test program. Laminar conditions existed on the smooth model at each of the test Reynolds numbers. The average value of the data appears to be about 10 percent higher than the laminar theoretical solution in the low Reynolds number case (Fig. 7a) and about 5 percent higher in the high Reynolds number case (Fig. 7b). This trend is probably caused by viscous induced pressure increases which are not taken into account in the theoretical calculations.

Variation of the heat-transfer distributions with small angles of attack is shown in Figs. 8 and 9 for both laminar (smooth model) and turbulent distributions. At $\alpha = 2$ deg the laminar windward heating rate (Fig. 8) near the model base is approximately 80 percent greater than at $\alpha = 0$. The effect of angle of attack on a typical turbulent heat-transfer distribution is shown in Fig. 9 for $Re_{\infty,L} = 6.2 \times 10^6$.

4.1.1 Passive Trips

Passive trip configuration comparisons are presented in Figs. 10 through 13, illustrating the individual contributions of (1) trip height, (2) number of rows, (3) trip spacing, and (4) axial trip location on boundary-layer transition and uniformity of the heating distribution. These data are all for $\alpha = 0$, with the heat-transfer rates (except for the trip-spacing comparisons) obtained from an instrumented ray directly behind a trip element.

Trip height required to produce transition for narrow-spaced passive trips at $S/R_n = 4.5$ is shown in Fig. 10 for $Re_{\infty,L} = 6.2 \times 10^6$. Axial heat-transfer distributions are shown for one, three, and ten rows of trips (Figs. 10a, b, and c). For the one-row configuration (Fig. 10a) the minimum height tested ($k = 0.100$ in.) produced a turbulent heating rate over the entire model length aft of the trips. Smaller trip heights were tested on the three-row and ten-row configurations. In these cases the smallest trip height which resulted in a nearly uniform turbulent heating level also was $k = 0.100$ in., regardless of the number of rows. These results are in close agreement with predictions for three-dimensional roughness made on the basis of the paper by Potter and Whitfield (Ref. 9). That method predicts a minimum transition distance well ahead of the first gage for a trip height of 0.1 in. at $Re_{\infty,L} = 6.2 \times 10^6$ and $S/R_n = 4.5$.

The ideal trip would produce a uniform turbulent boundary layer aft of the trip location and a constant circumferential heat-transfer rate at

any axial location at zero angle of attack. However, discrete disturbances are introduced by the trips, forming wedges of turbulence behind the trip elements. These wedges merge to form a uniform heating distribution farther downstream of the trips. A visual illustration of the flow disturbances produced by the trips is shown by oil flow photographs in Fig. 11. Figure 12 shows the effect of circumferential trip spacing on the longitudinal heat-transfer distribution uniformity at several radial values for passive narrow- and wide-spaced trips. In each case the heat-transfer distribution becomes essentially uniform for $S/Rn \geq 20$. The total non-uniformity is illustrated by the dashed lines in Fig. 12a for the narrow-spaced configuration and is compared to the data for the wide-spaced configuration (Fig. 12b). The heat-transfer distribution produced by the narrow-spaced configuration is clearly more uniform than that of the wide-spaced configuration.

The majority of the tests were performed with trips located at an axial station of $S/Rn = 4.5$. Additional data were taken with trips located at $S/Rn = 8.5$ to evaluate the influence of trip location on trip effectiveness. Data from narrow three-row trip configurations are presented in Fig. 13 for a trip height of $k = 0.100$ in. These data indicate that the transition length for the forward trip is about half that obtained from the aft trip. The shorter transition length is probably the result of the thinner boundary layer at the forward trip (i.e., the trip effectiveness is a function of the ratio of trip height to boundary-layer thickness).

The effect of Reynolds number on transition for narrow-spaced passive trips at $S/Rn = 4.5$ is presented in Fig. 14 for three different configurations (one row, $k = 0.100$ in.; three rows, $k = 0.150$ in.; ten rows, $k = 0.150$ in.). All configurations indicate a nearly laminar heating level over the entire model for $Re_{\infty,L} = 2.2 \times 10^6$, and transition to a fully turbulent level over the model at $Re_{\infty,L} = 6.2 \times 10^6$. The data just aft of the trips for the ten-row configuration are significantly lower than the theoretical laminar solution for the lowest Reynolds number and are indicative of a disturbed flow region near the trips.

4.1.2 Active Trips

Active trip configuration comparisons are presented in Figs. 15 and 16, illustrating the individual contributions of (1) trip height (mass injection rate), (2) number of rows (or magnitude of mass injection), and (3) trip spacing (orifice spacing) on boundary-layer transition and uniformity of the heating distributions. These data are all for $u = 0$.

Heat-transfer rates for the longitudinal plots of Fig. 15 were obtained from instrumentation at the same radial location (same θ) as an orifice (see Fig. 4a). Computed effective trip heights for the various injection rates are included in Fig. 15. Data for one-, three-, and ten-row configurations are presented. The one-row configuration (Fig. 15a) has a laminar distribution over the entire model for $k' \leq 0.021$ in. with maximum heat-transfer rate near the trip being attained for $k' = 0.150$ in. An additional increase of trip height to $k' = 0.261$ in. significantly reduces the heat-transfer rate over the entire model. The reduction in heating rate for $k' = 0.261$ in. (largest mass injection rate) indicates that the large mass injection rate is "cooling" the model surface. For $S/Rn \geq 25$ the effects of trip height (for the range $k' = 0.032$ to 0.150 in.) are insignificant. Similar variations with trip height are shown in Figs. 15b and c for three- and ten-row configurations; however, transition occurs at significantly lower effective trip heights (lower mass injection rate) than for the one-row configurations, suggesting that the number of rows strongly influences the heat-transfer distribution for active trips. A fully turbulent heating distribution immediately aft of the trip location was never attained for any active configuration. Apparently, a "transpiration cooling" or "blowing" effect reduces the heating level just aft of the trip locations.

Effects of orifice spacing on heat-transfer distribution uniformity are shown in Fig. 16 for one row of active trips at $S/Rn = 4.5$. In this figure the ratio of Stanton number to the theoretical (Ref. 7) Stanton number was used to indicate the deviation from the desired turbulent heating

level. Each of the circumferential heating distributions shows that, by comparison with the wide-spaced trips, the narrow-spaced trips ($\theta_g = 20$ deg) give results closer to the turbulent level and considerably more uniform at all axial stations.

4.2 FORCE TESTS

Comparisons of the static aerodynamic force and moment characteristics of the passive configurations are presented in Fig. 17 for the maximum test Reynolds number ($Re_{\infty, L} = 6.2 \times 10^6$). Data for the smooth model are shown for comparison. The stability characteristics of all configurations were virtually identical, although a small effect of the trips was obtained on the model center-of-pressure location. With the exception of the ablated trip configuration (configuration A1020-0103-0505), the axial-force coefficients are about the same for all trip configurations and are higher (by an almost constant amount) than the smooth model data. The higher axial force is indicative of a turbulent boundary layer (increased skin friction) existing on the model but also includes an unknown increment produced by the trip itself. An asymmetric variation in axial force is noted for the ablated configuration (an asymmetric trip) with significant increase above the smooth model data for increasing negative angles of attack. A theoretical point (flagged symbol) is shown for comparison at $\alpha = 1$ deg. The theoretical result was obtained by the method of Ref. 10 for an assumed laminar boundary layer and includes the viscous contribution. Smooth model stability data show excellent agreement with the theory, and the smooth model axial-force coefficient is approximately 7 percent higher than the theory, which is larger than the quoted uncertainty (± 4.6 percent) of the axial-force measurement.

Similar aerodynamic characteristics are presented for active configurations in Fig. 18, with the smooth model data shown for comparison. The stability data for all configurations (as for the passive configurations) are virtually identical to the smooth model data. The axial-force coefficient

variation with angle of attack for the one-row configuration (3020-0101-0000), which has the lowest mass injection rate, is approximately the same as that of the smooth model data. The three-row configurations show an increase in axial-force coefficient (compared to the smooth model) for most angles of attack with a "flattening" of the curve noted in the region of $\alpha = -4$ to 4 deg. Heat-transfer data (Fig. 15) for these configurations have indicated (1) transition to a turbulent boundary layer at the base of the model for the one-row configuration and (2) the existence of a turbulent boundary layer over the aft third of the model for a three-row configuration (3020-0303-0000).

Effect of Reynolds number on the axial-force coefficient at $\alpha = 0$ for a passive configuration (1020-0505-1010) is presented in Fig. 19. The data show the axial force to be essentially the same as that for the smooth model for $Re_{\infty,L} \leq 4.8 \times 10^6$, with a significant increase in axial force at the maximum test Reynolds number ($Re_{\infty,L} = 6.2 \times 10^6$). The sudden rise in axial force suggests that transition to a turbulent boundary layer on the model has occurred at this Reynolds number; however, additional data at higher Reynolds numbers would be needed to confirm this. Form drag contribution of the trips was not measurable at the lower Reynolds numbers, since the data with trips were essentially the same as the smooth model data.

Axial-force coefficient data at $\alpha = 0$ are presented in Fig. 20 to show the effects of mass injection rate and Reynolds number for an active trip configuration. The data for the active configuration were ratioed to the smooth model coefficient (data fairing of Fig. 19), thus providing a direct comparison to the smooth model (laminar data). For each Reynolds number, the active configuration data were nearly the same as the smooth model data at the lowest mass injection rates (ratio ≈ 0.98); with sufficient mass injection the ratio increased to approximately 1.08. Comparison of the data at maximum and minimum Reynolds numbers ($Re_{\infty,L} = 6.2 \times 10^6$ and $Re_{\infty,L} = 2.1 \times 10^6$) indicates that the deviation from the smooth model axial force occurs at a significantly lower mass injection rate for the maximum Reynolds number.

5.0 CONCLUDING REMARKS

Heat-transfer and static stability tests were conducted on a blunt cone model (TDV geometry) to obtain data for the design of effective boundary-layer trips for the control of transition-induced dispersion for a reentry vehicle. The free-stream Reynolds number, based on the total model length, was varied from 1.5 to 6.2 million at a free-stream Mach number of 10. Angle of attack was from 0 to 2 deg for the heat-transfer tests and from -7.5 to 7.5 deg for the static stability tests. Based on the results presented, the following observations are made:

1. Smooth model heat-transfer data were repeatable and laminar at all test conditions. The data agreed with laminar theory within ± 10 percent.
2. Minimum passive trip height, k , required to produce a turbulent heating level "close" to the trip was $k = 0.100$ in. at $Re_{\infty, L} = 6.2 \times 10^6$, regardless of the number of rows, in very good agreement with prediction.
3. The narrow-spaced trips ($\theta_s = 20$ deg), both passive and active, generated a more uniform radial heat-transfer distribution than the wide-spaced trips ($\theta_s = 40$ deg).
4. Transition length for a passive trip at the forward trip location ($S/R_n = 4.5$) was about half the length obtained for an equivalent trip height located at the aft trip location ($S/R_n = 8.5$). The thicker boundary layer, slightly lower local Reynolds number, and slightly higher local Mach number at $S/R_n = 8.5$ probably contributed to that result.

5. A fully turbulent heating distribution immediately aft of the trip location was never attained for any active configuration. Apparently, a "transpiration cooling" effect occurred to reduce the heating level just aft of the trip locations.
6. Static stability of the model was not affected by any of the trip configurations, and the data showed excellent agreement with theory at $\alpha = 1$ deg.

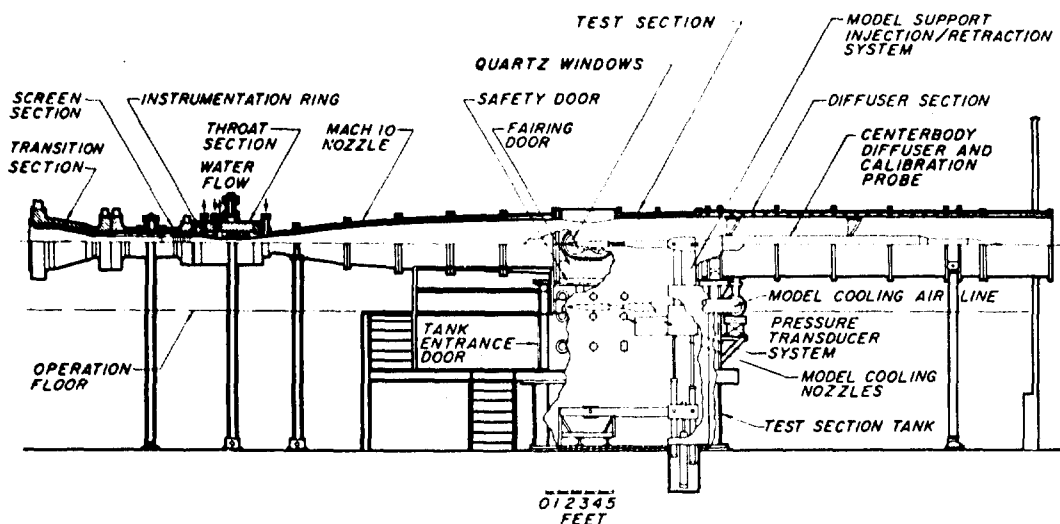
REFERENCES

1. Test Facilities Handbook (Tenth Edition). "von Kármán Gas Dynamics Facility, Vol. 3." Arnold Engineering Development Center, May 1974.
2. Stone, David R. and Carey, Aubrey M., Jr. "Discrete Sonic Jets Used as Boundary-Layer Trips at Mach Numbers of 6 and 8.5." NASA TN D-6802, July 1972.
3. Spaid, F. W. and Cassell, L. A. "Aerodynamic Interference Induced by Reaction Controls." AGARDOGRAPH No. 173, McDonnell Douglas Corporation, Huntington Beach, Calif., December 1973.
4. Cook, W. J. and Felderman, E. J. "Reduction of Data from Thin-Film Heat-Transfer Gages: A Concise Numerical Technique." AIAA Journal, Vol. 4, No. 3, March 1966, pp. 561-562.
5. Fay, J. A. and Riddell, F. R. "Theory of Stagnation Point Heat Transfer in Dissociated Air." Journal of the Aeronautical Sciences, Vol. 25, No. 2, February 1958, pp. 73-85, 121.
6. Patankar, S. V. and Spaulding, D. B. Heat and Mass Transfer in Boundary Layers: A General Calculation Procedure. CRC Press, Cleveland, 1968.

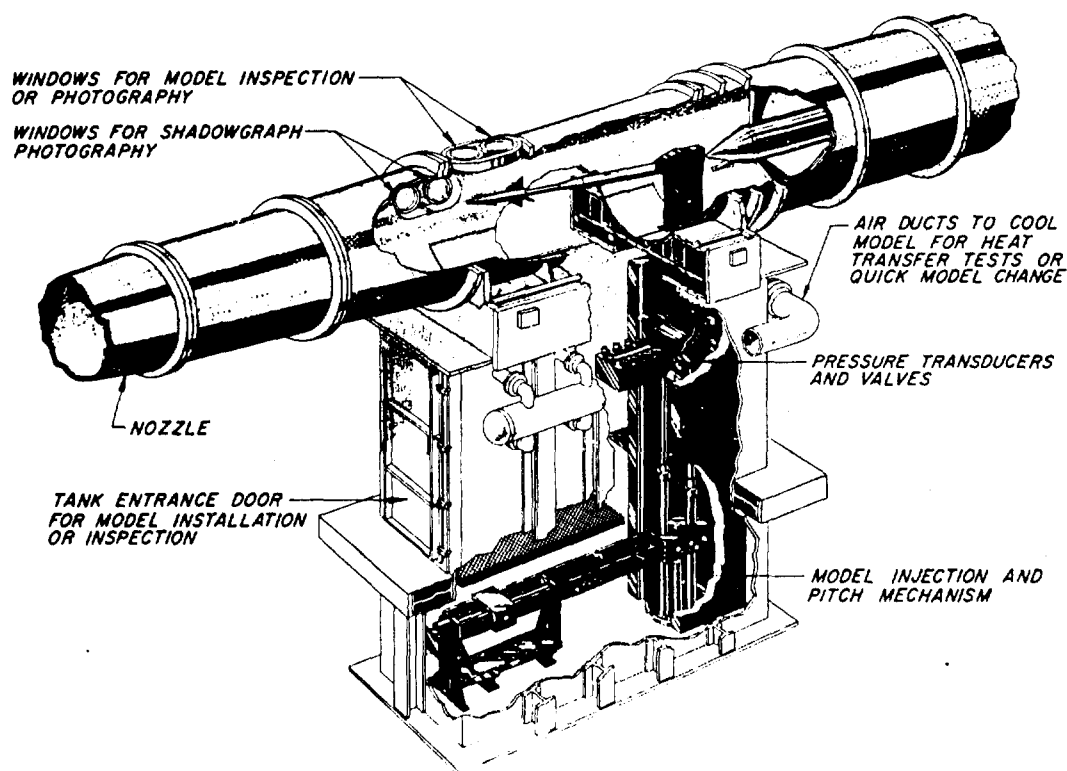
7. Mayne, Arlos W., Jr. and Dyer, D. F. "Comparisons of Theory and Experiment for Turbulent Boundary Layers on Simple Shapes at Hypersonic Conditions." Proceedings of the 1970 Heat Transfer and Fluid Mechanics Institute, Stanford University Press, 1970, pp. 168-188.
8. Inouye, M., Rakich, J. V., and Lomax, H. "A Description of Numerical Methods and Computer Programs for Two-Dimensional and Axisymmetric Supersonic Flow over Blunt-Nosed and Flared Bodies." NASA TN D-2970, August 1965.
9. Potter, J. Leith and Whitfield, Jack D. "Effects of Slight Nose Bluntness and Roughness on Boundary-Layer Transition in Supersonic Flows." Journal of Fluid Mechanics, Vol. 12, Part 4, April 1962, pp. 501-535.
10. Mayne, Arlos W., Jr. "Calculation of the Laminar Viscous Shock Layer on a Blunt Biconic Body at Incidence to Supersonic and Hypersonic Flow." AEDC-TR-76-123 (ADA033225), December 1976.

PRECEDING PAGE BLANK

AEDC-TR-76-157



Tunnel Assembly



Tunnel Test Section

Figure 1. Tunnel C.

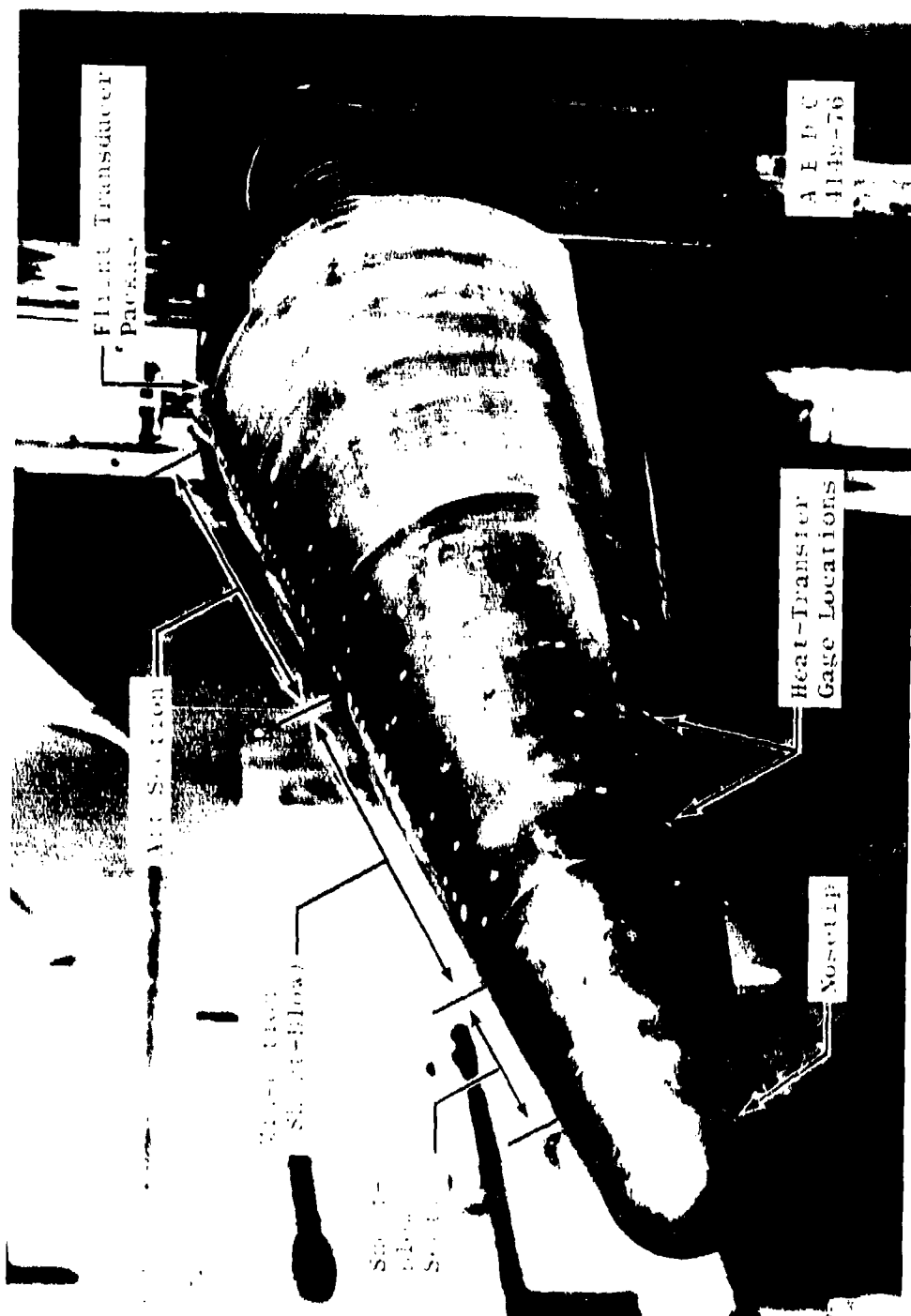
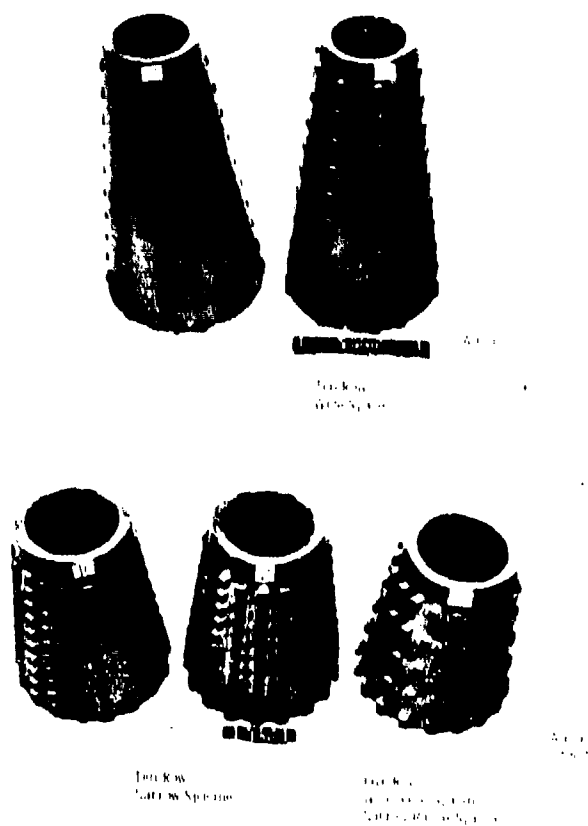
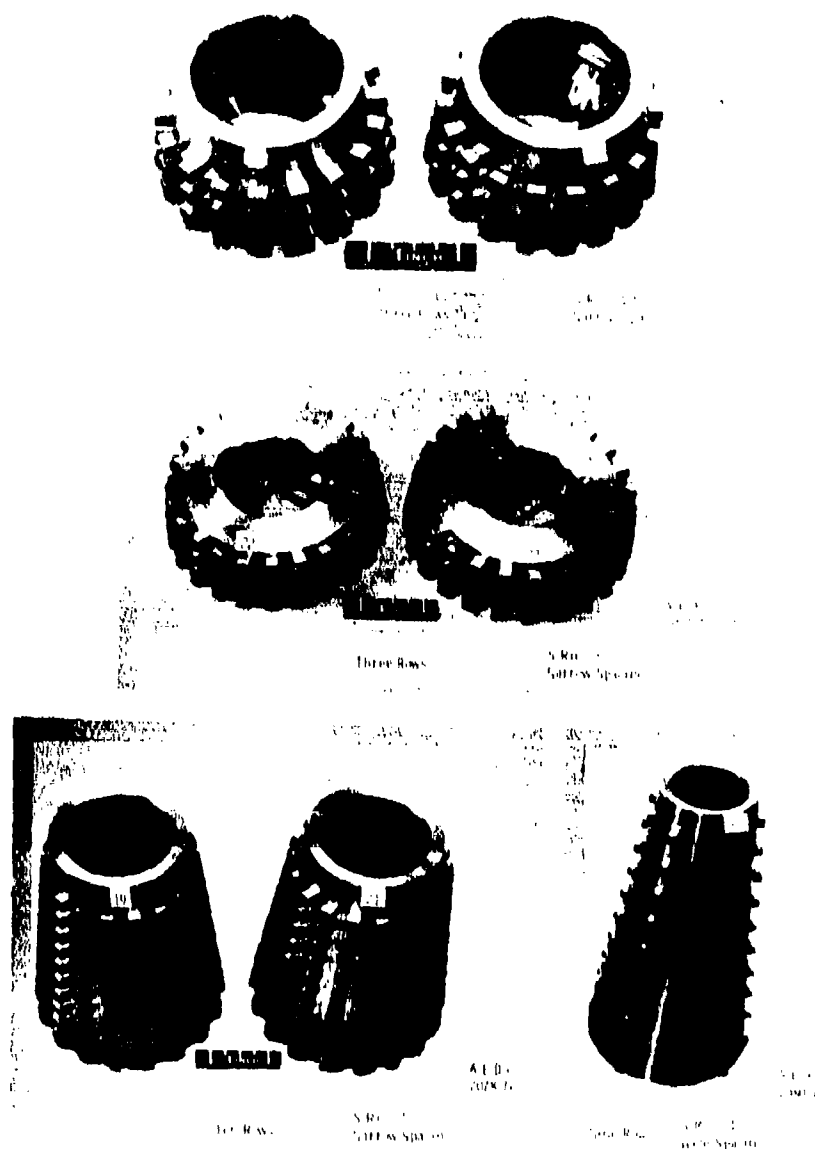


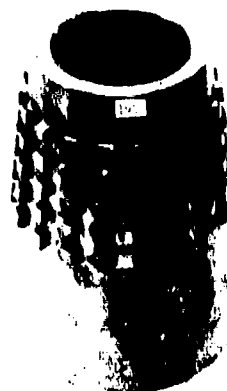
Figure 2. Photograph of model in Tunnel C tank.



**b. Multiple-row passive trips at $S/R_n = 4.5$,
alternate heights on top and bottom
Figure 3. Continued.**



a. Symmetric passive trips
Figure 3. Continued.



Symmetric Five Row Trip

AEDC
Also 76

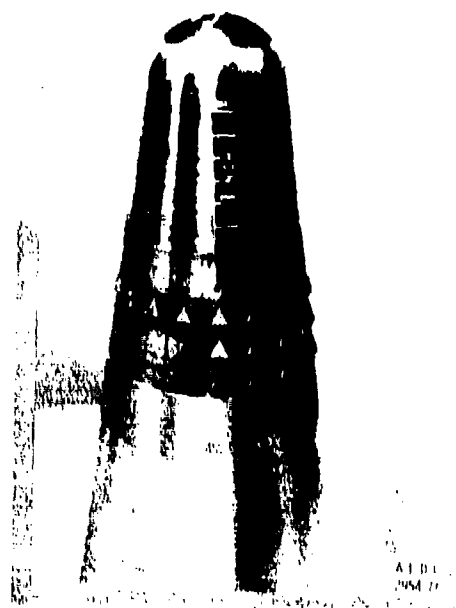


One and Three
Row Combination
Trip

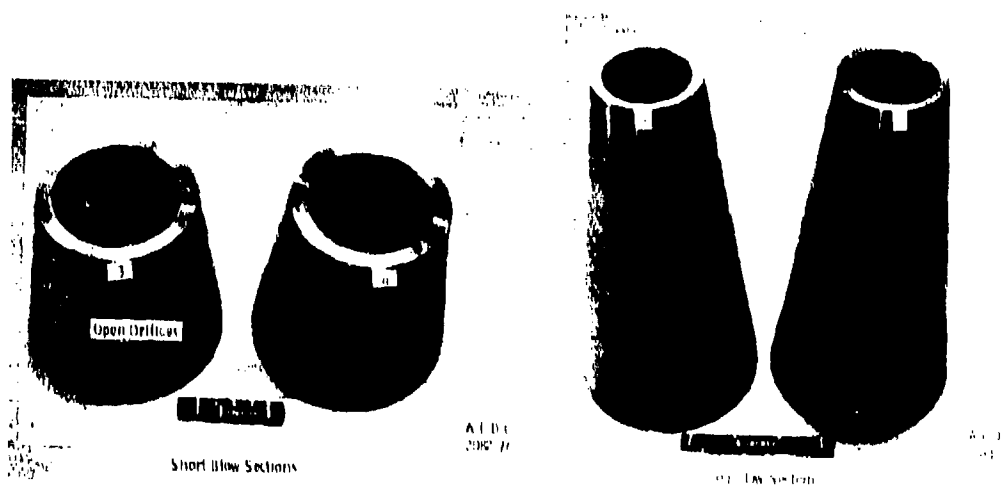
Symmetric Trips

AEDC
Also 76

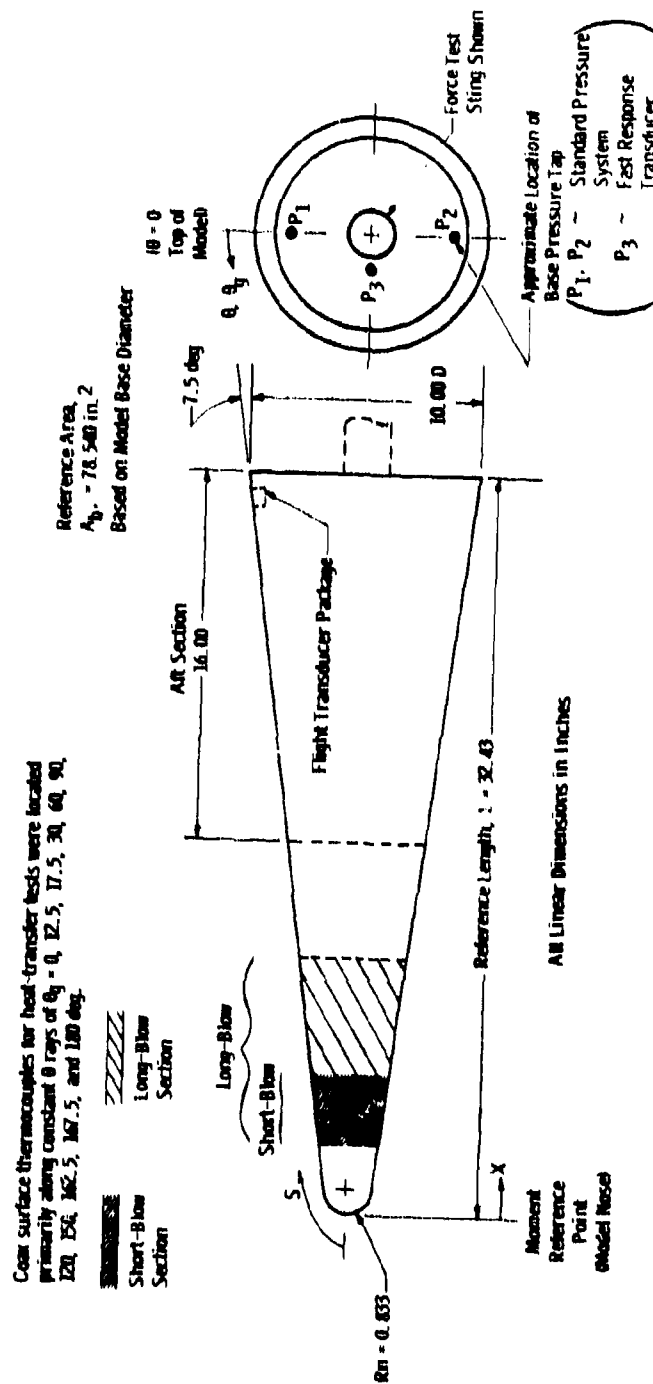
d. Modified passive trips
Figure 3. Continued.



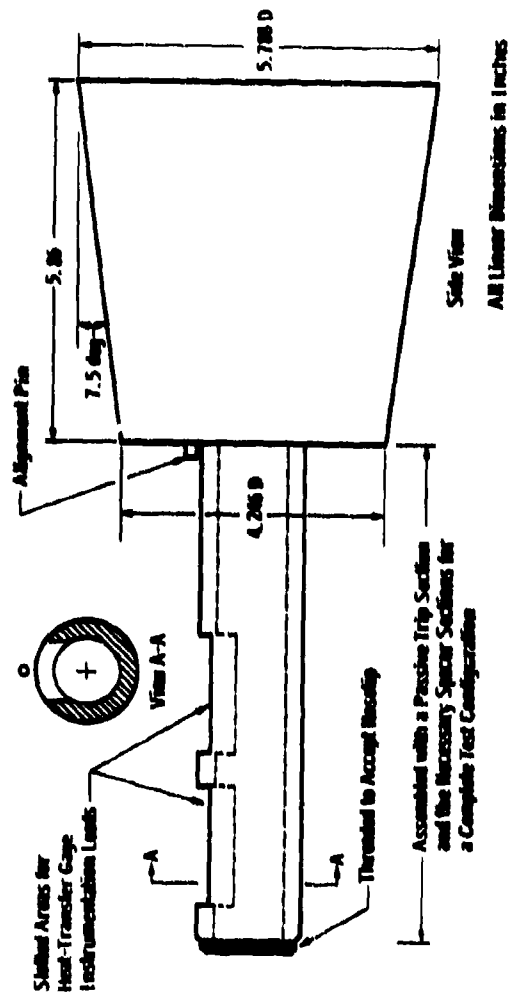
e. Ablated-passive trip configuration



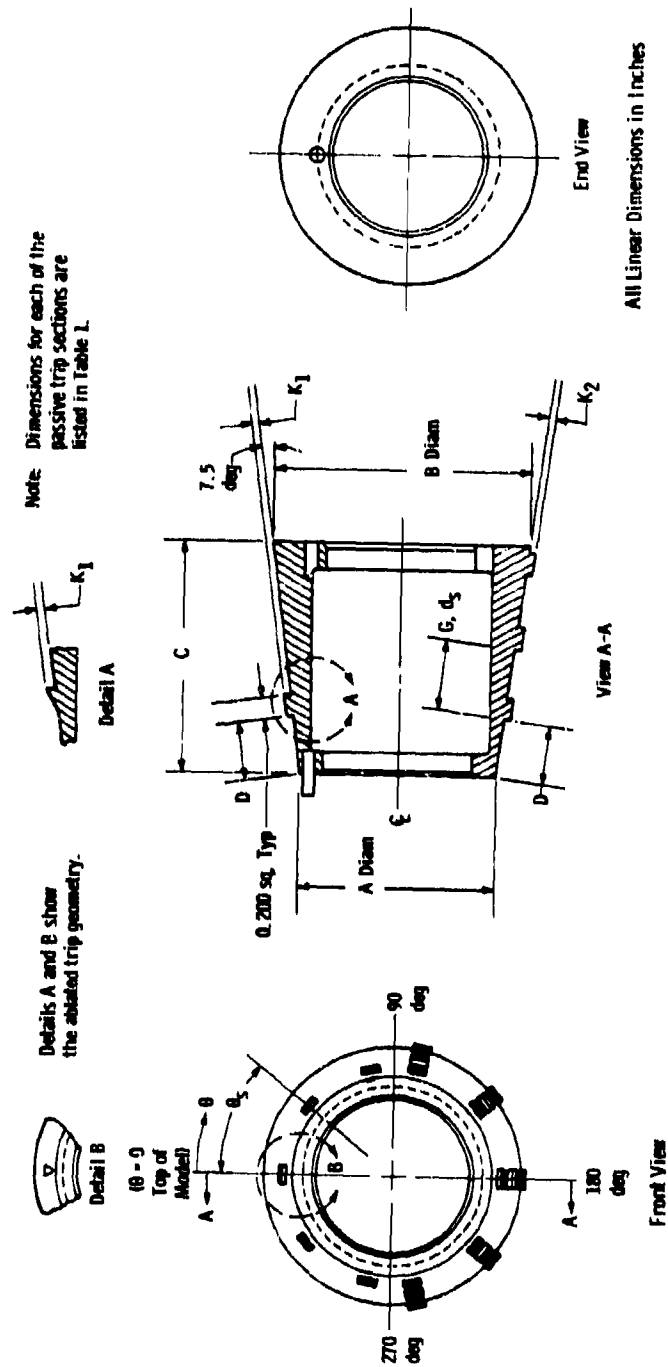
f. Active trip sections
Figure 3. Concluded.



a. Assembly
 Figure 4. Model details.

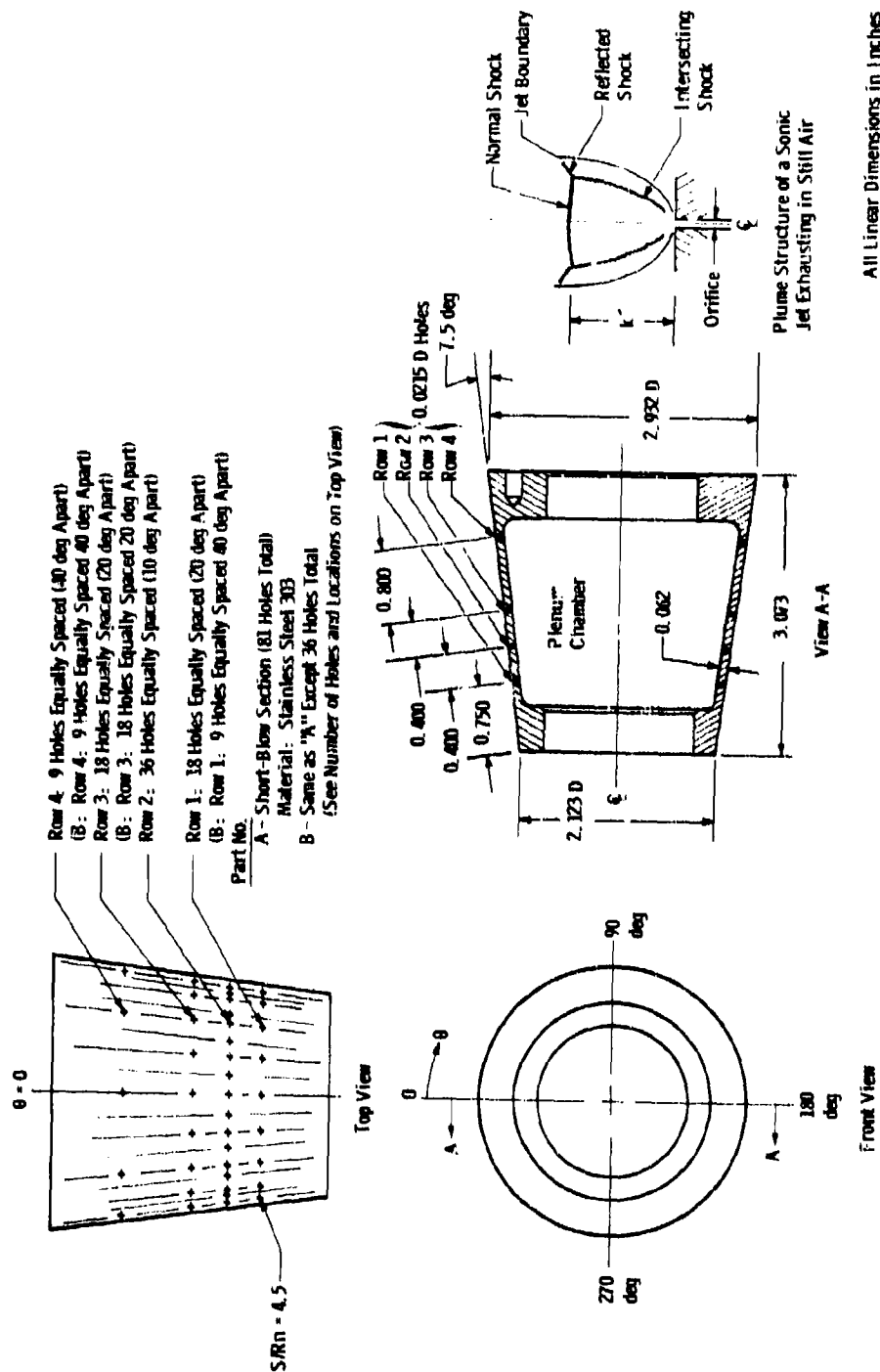


b. Midsection trip
Figure 4. Continued.

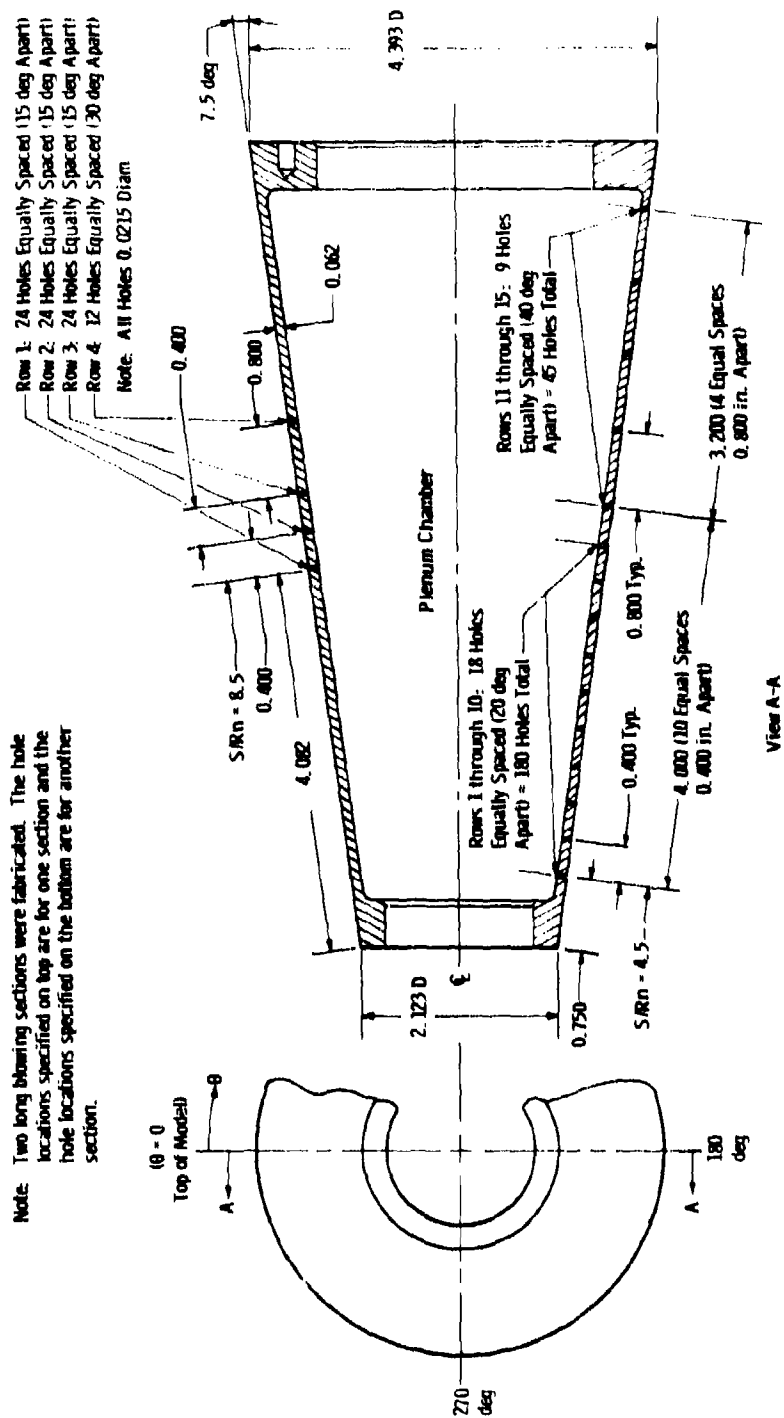


c. Trip section details
Figure 4. Continued.

All Linear Dimensions in Inches



d. Short-blow sections
 Figure 4. Continued.



e. Long-blow sections
Figure 4. Concluded.

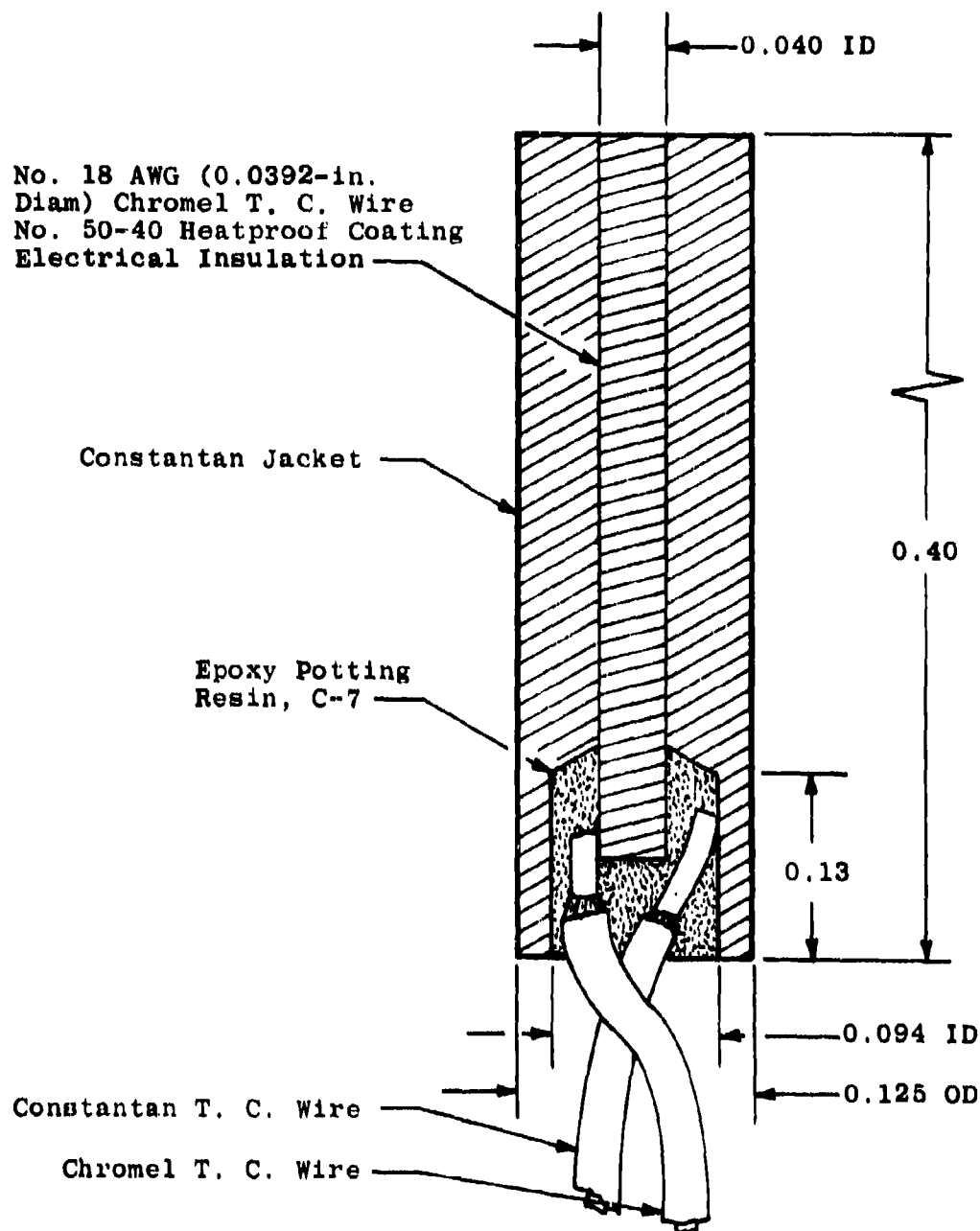
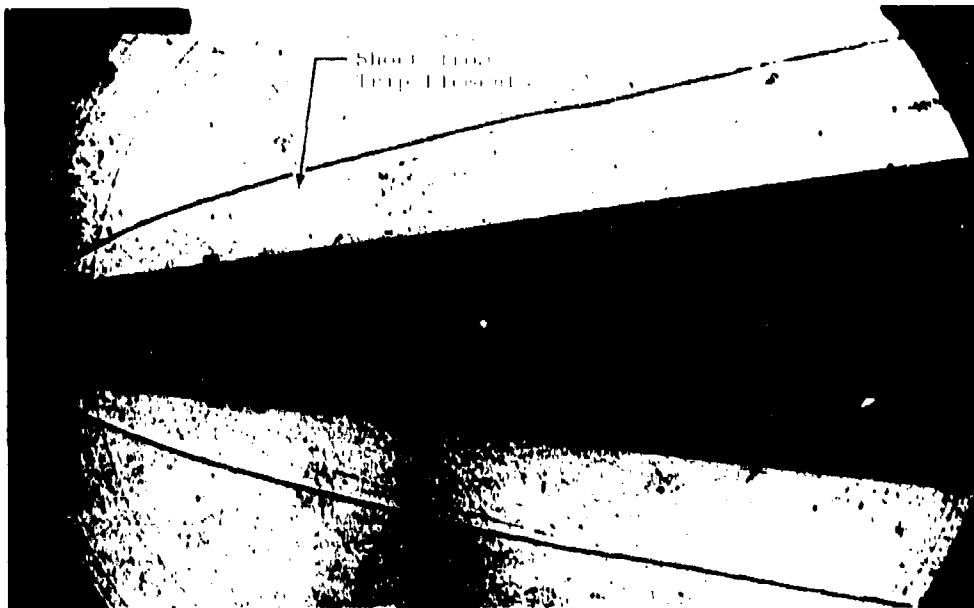
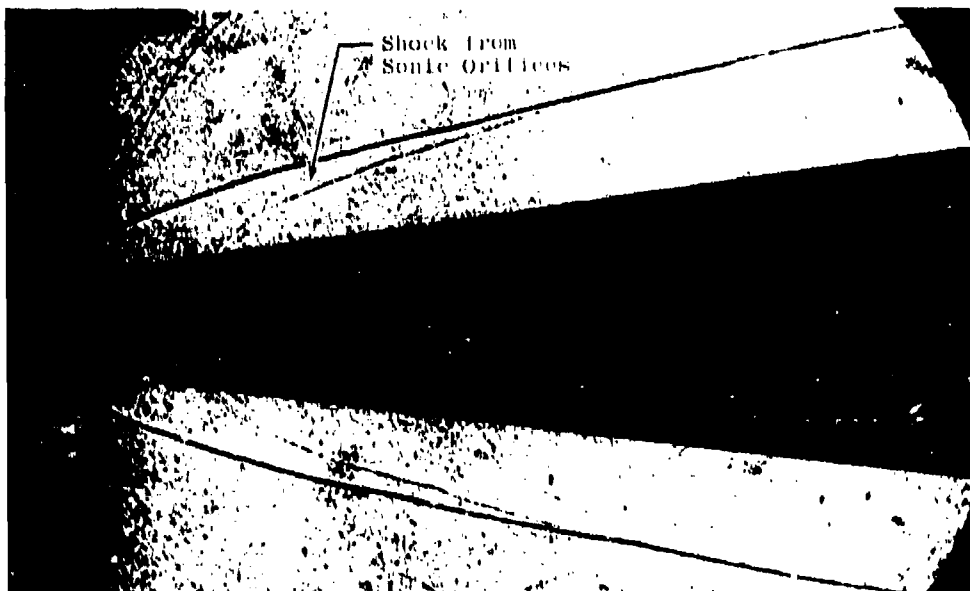


Figure 5. Chromel[®]-constantan coaxial surface thermocouple gage, 10X scale.



a. Passive configuration (1020-0103-1510), $k = 0.150$ in.
for top row



b. Active configuration (1020-0101-0000), $k' = 0.15$ in.
Figure 8. Typical shadowgraphs, $Re_{\infty L} = 6.2 \times 10^6$, $\alpha = 0$.

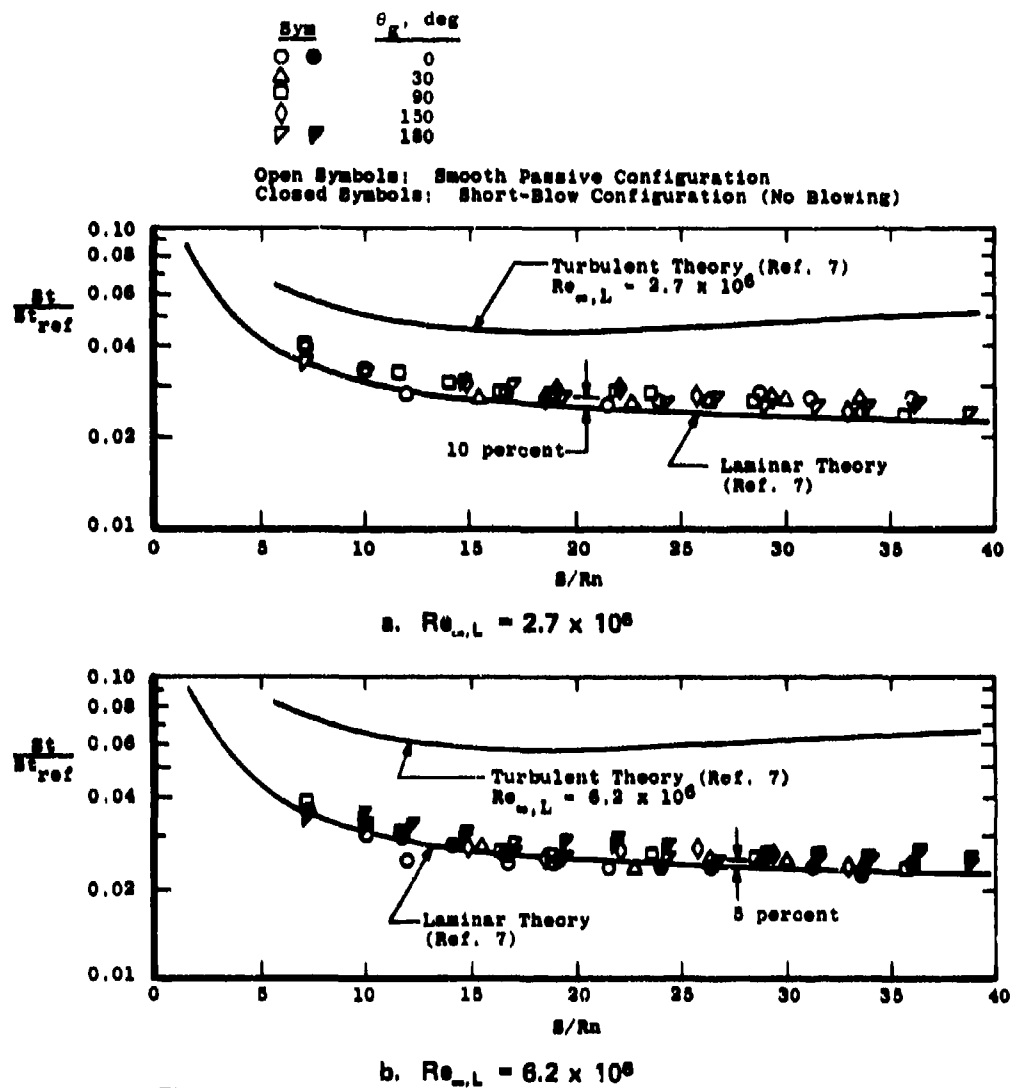
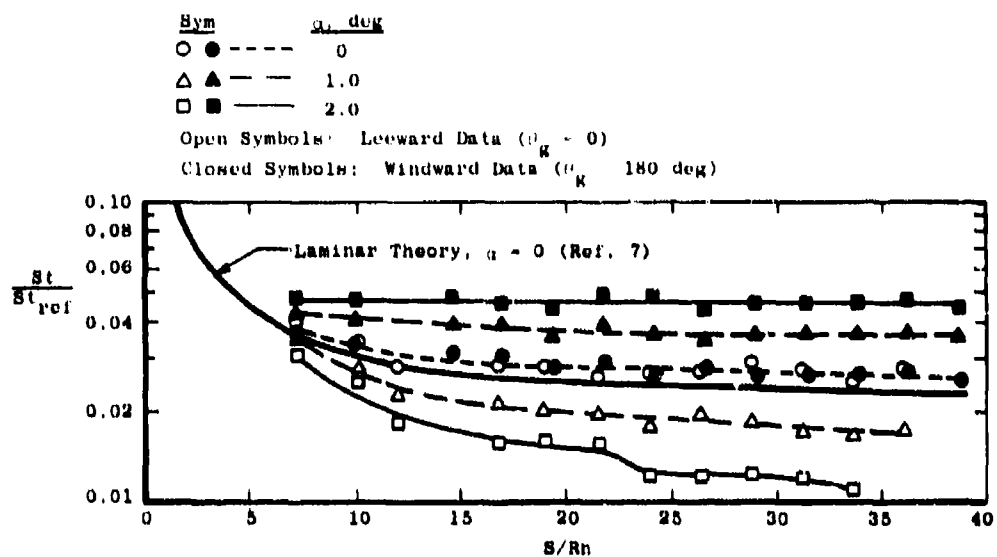
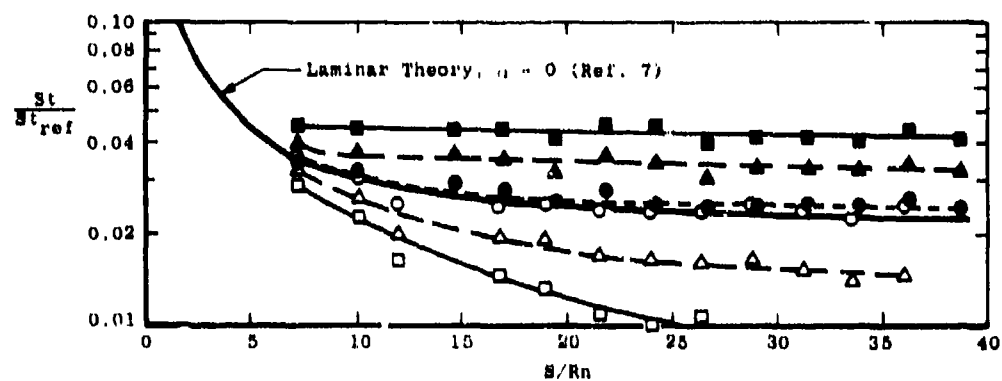


Figure 7. Comparison of smooth model heat-transfer data to theory at $\alpha = 0$.



a. $Re_{\infty, L} = 2.7 \times 10^6$



b. $Re_{\infty, L} = 6.2 \times 10^6$

Figure 8. Effect of angle of attack on the smooth model heat-transfer distribution.

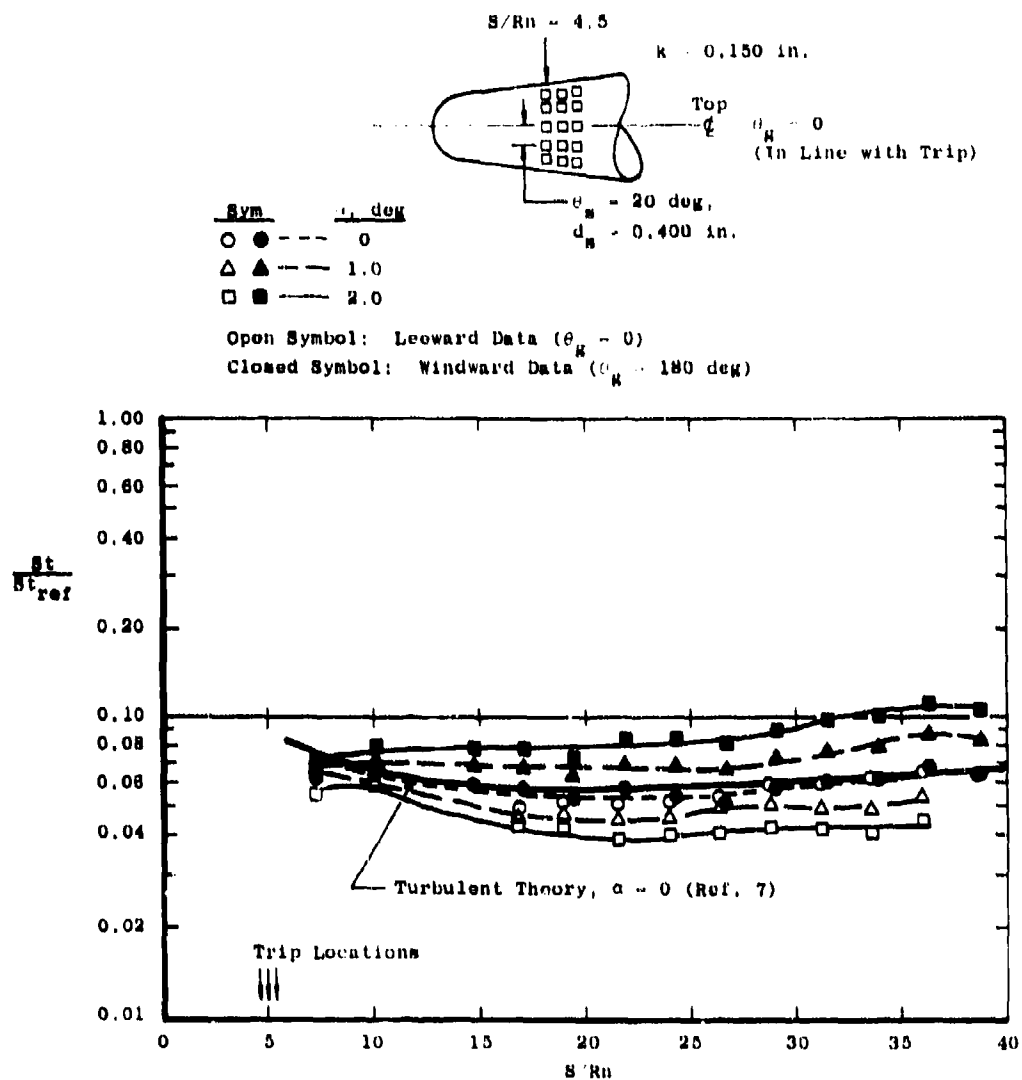


Figure 9. Effect of angle of attack on a turbulent heat-transfer distribution (configuration 1020-0303-1515), $Re_{\infty,L} = 6.2 \times 10^6$.

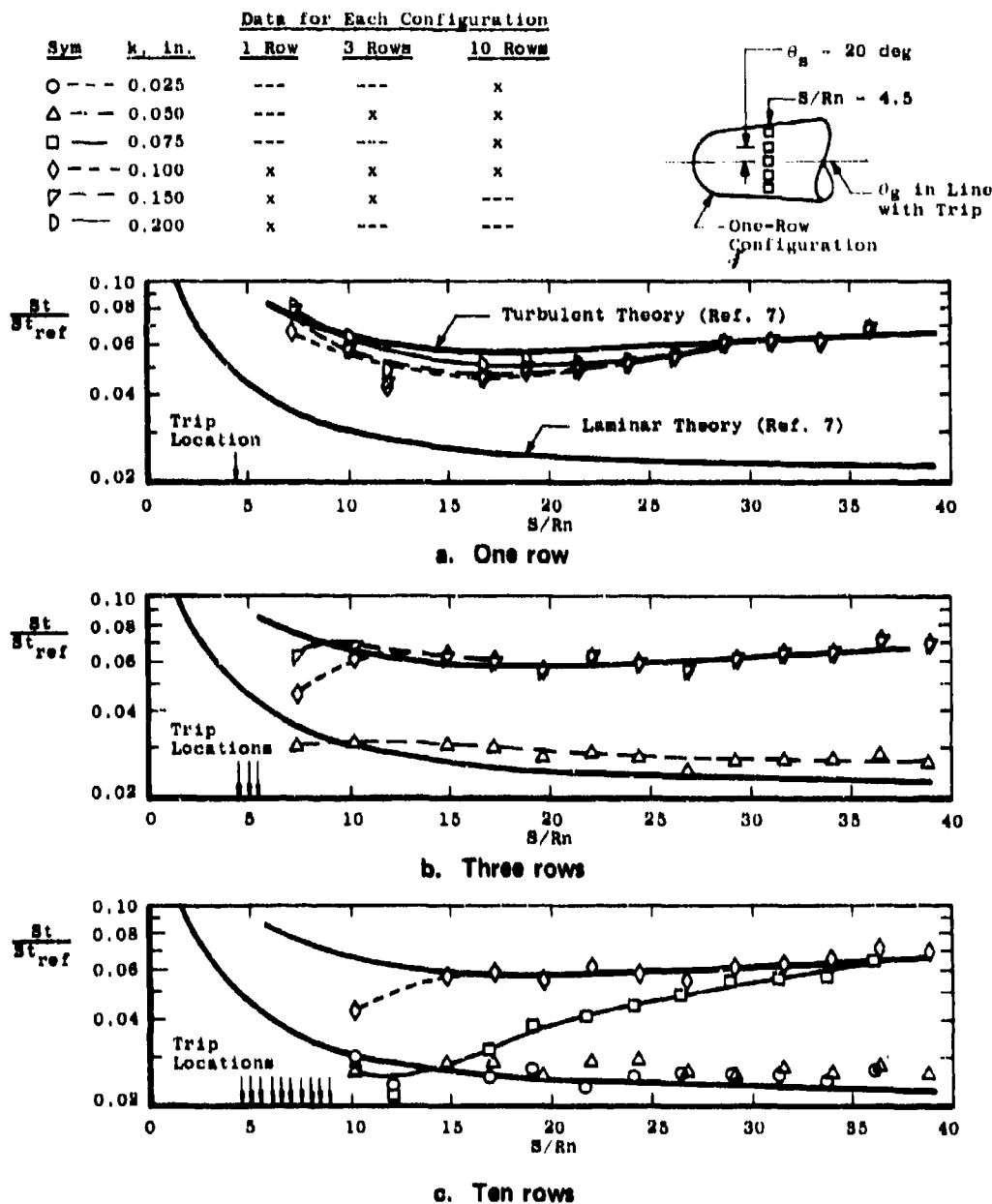


Figure 10. Effect of trip height and number of rows on transition at $Re_{x,L} = 6.2 \times 10^6$, narrow-spaced passive trips at $S/Rn = 4.5$.

Note: Oil was applied to model on the side opposite the heat-transfer cases to prevent interference with the instrumentation.



a. Passive configuration (1020-0303-1515), $\alpha = 2^\circ$
Figure 11. Typical oil flow photographs, $Re_{\infty} = 6.2 \times 10^5$.



b. Active configuration (3120-0303-0000), $k' = 0.068$ in.,
 $P_e = 7.0$ psia, $\dot{m} = 0.0024$ lbm/sec, $\alpha = 0$
Figure 11. Concluded.

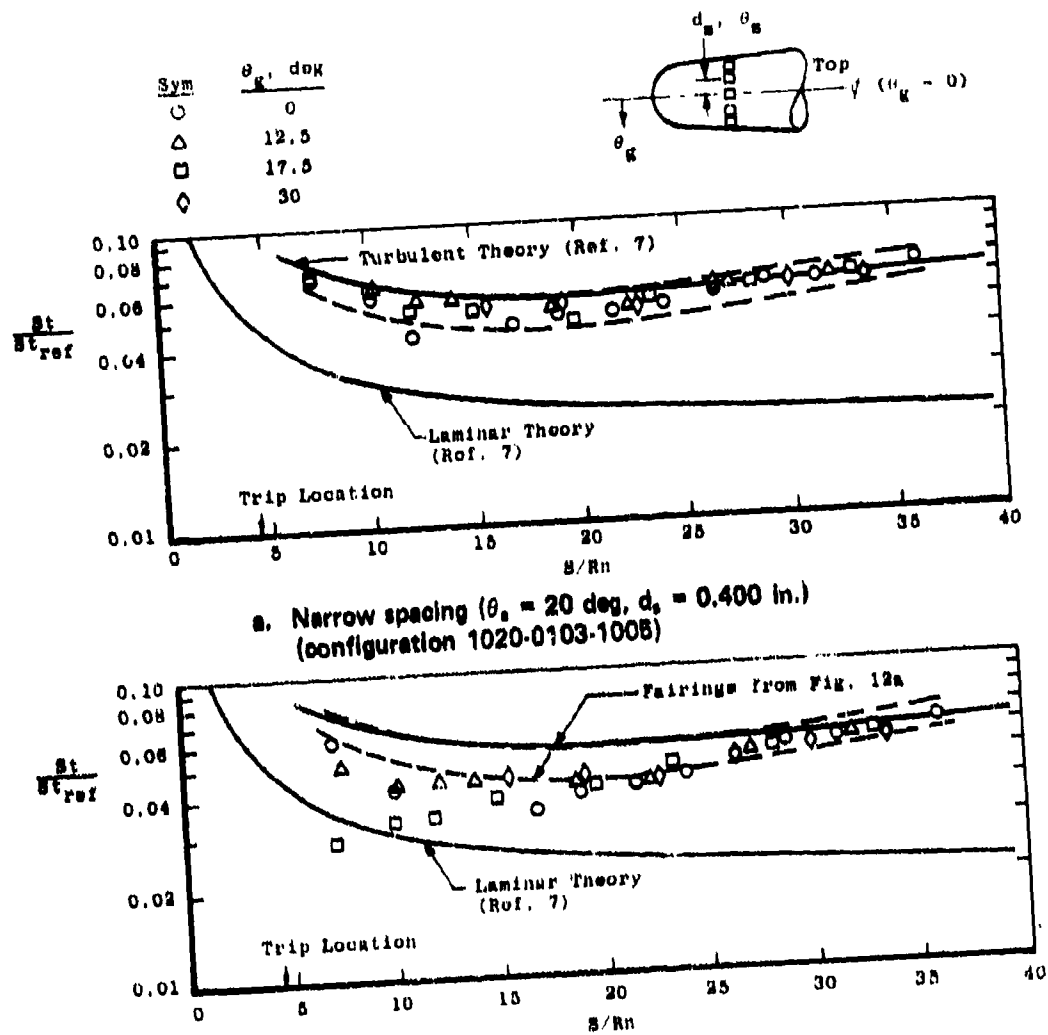


Figure 12. Effect of circumferential trip spacing on the heat-transfer distribution uniformity for passive trips, one row at $S/Rn = 4.5$, $k = 0.100$ in., $Re_{\infty L} = 6.2 \times 10^5$.

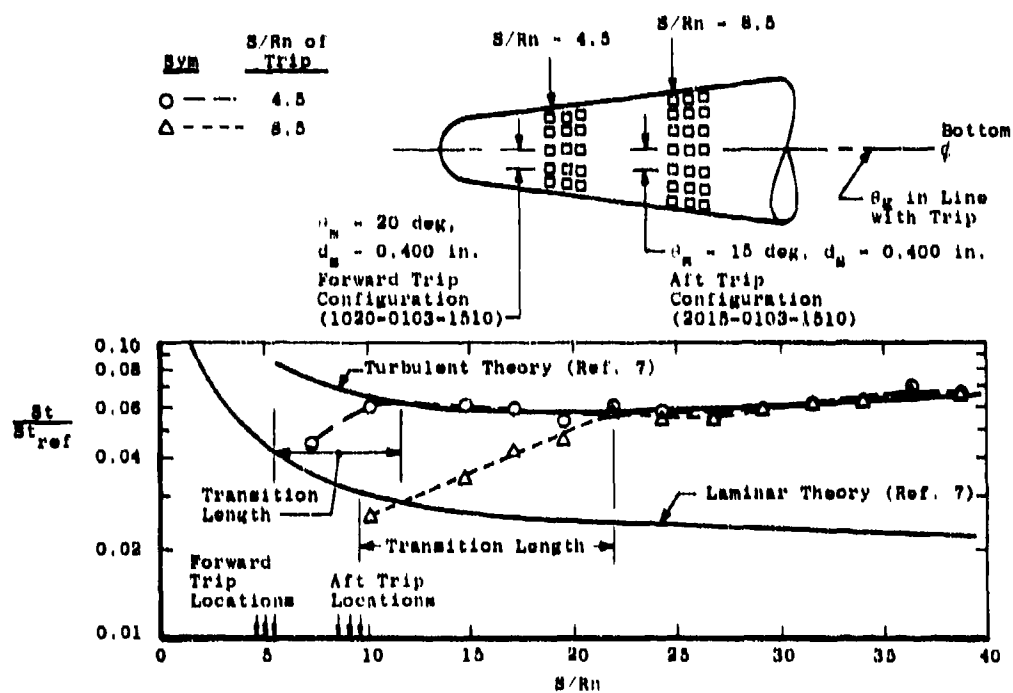


Figure 13. Effect of axial trip location on transition length,
 three rows of narrow-spaced passive trips, $k = 0.100$ in.,
 $Re_{u,L} = 6.2 \times 10^6$.

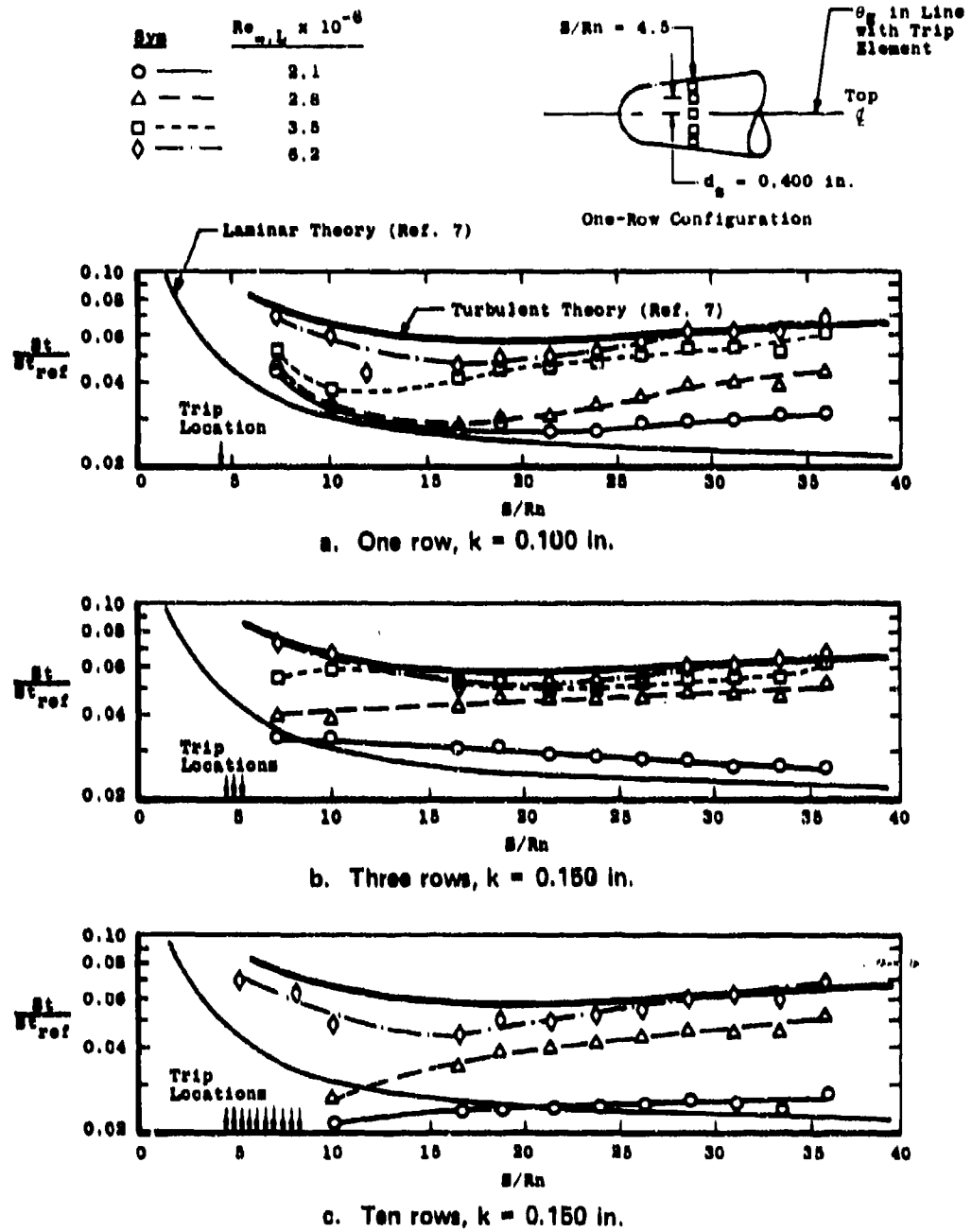
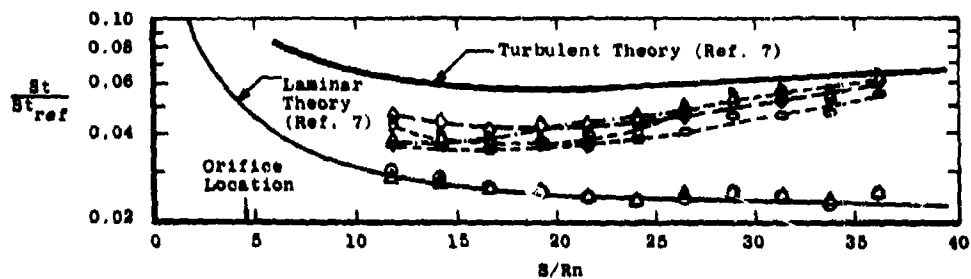
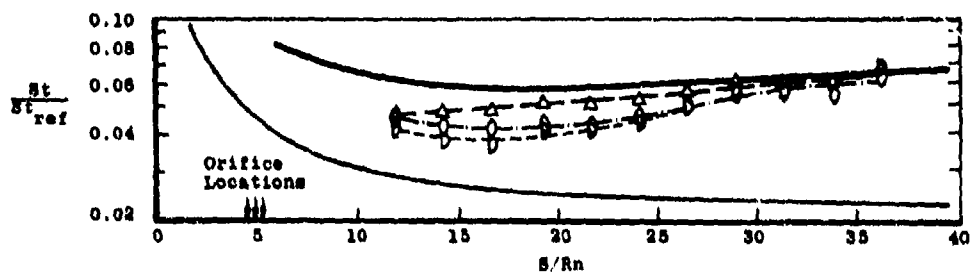


Figure 14. Effect of Reynolds number on transition, narrow-spaced passive trips at $S/Rn = 4.5$.

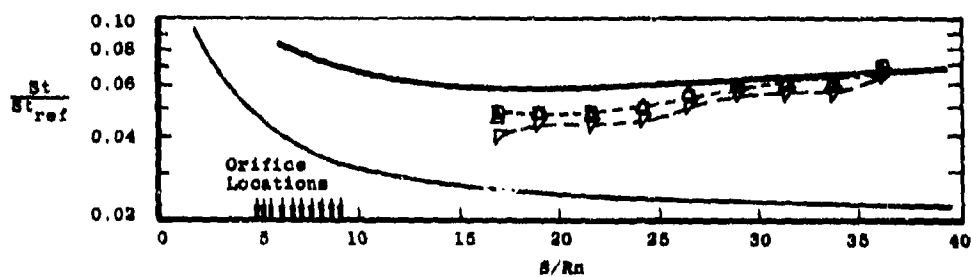
Sym	k', in.	P _c , psia	m per Row, lbm/sec	Data for Each Configuration		
				1 Row	3 Rows	10 Rows
○	0	0	0	x	---	---
△	0.021	0.7	0.00007	x	x	x
□	0.026	1.0	0.00010	---	---	x
◇	0.032	1.5	0.00016	x	---	---
○	0.037	2.0	0.00022	---	---	x
○	0.050	3.7	0.00040	x	x	---
○	0.070	7.0	0.00081	---	x	---
○	0.150	32.7	0.0036	x	---	---
○	0.261	100	0.0135	x	---	---



a. One row (configuration 3020-0101-0000)



b. Three rows (configuration 3020-0303-0000)



c. Ten rows (configuration 3020-1010-0000)

Figure 15. Effect of trip height and number of rows on transition at $Re_{x,L} = 6.2 \times 10^6$, narrow-spaced active trips at $S/Rn = 4.5$.

Data were obtained at each of the axial locations by interpolation from axial heat-transfer distributions for all eleven rays of instrumentation. Multiple data points were obtained by assuming symmetry.

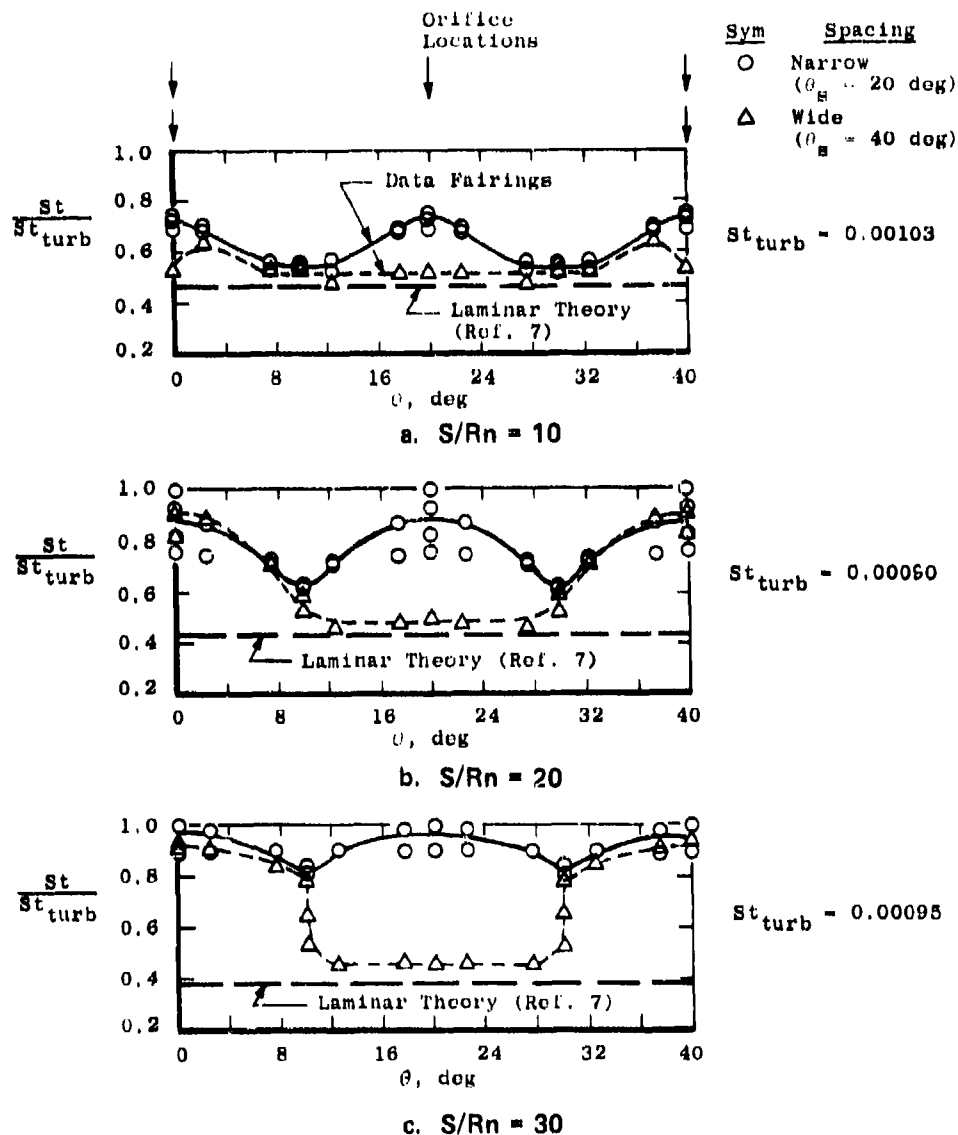


Figure 16. Effect of circumferential orifice spacing on the heat-transfer distribution uniformity for active trips, one row at $S/R_n = 4.5$, $k = 0.033$ in. ($p_e = 1.5$ psia), $Re_{m,L} = 6.2 \times 10^6$.

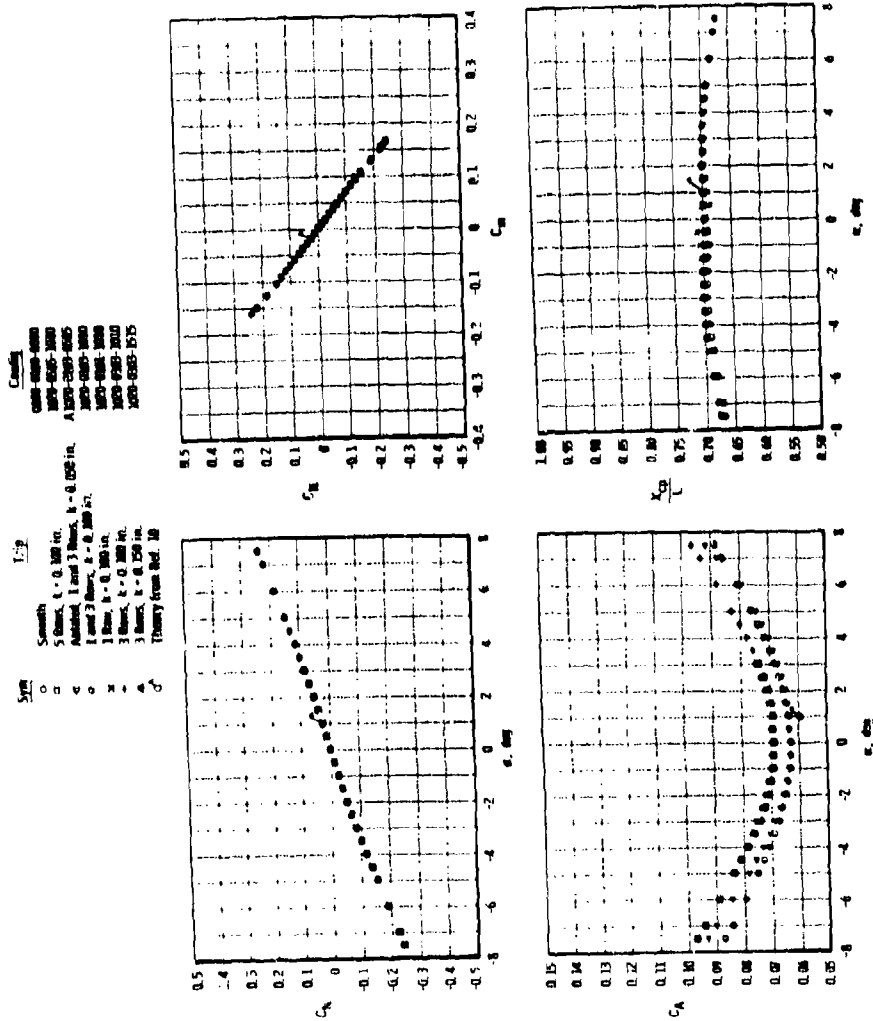


Figure 17. Effect of various passive trips on the longitudinal stability and axial-force characteristics, $Re_{\infty L} = 5.2 \times 10^6$.

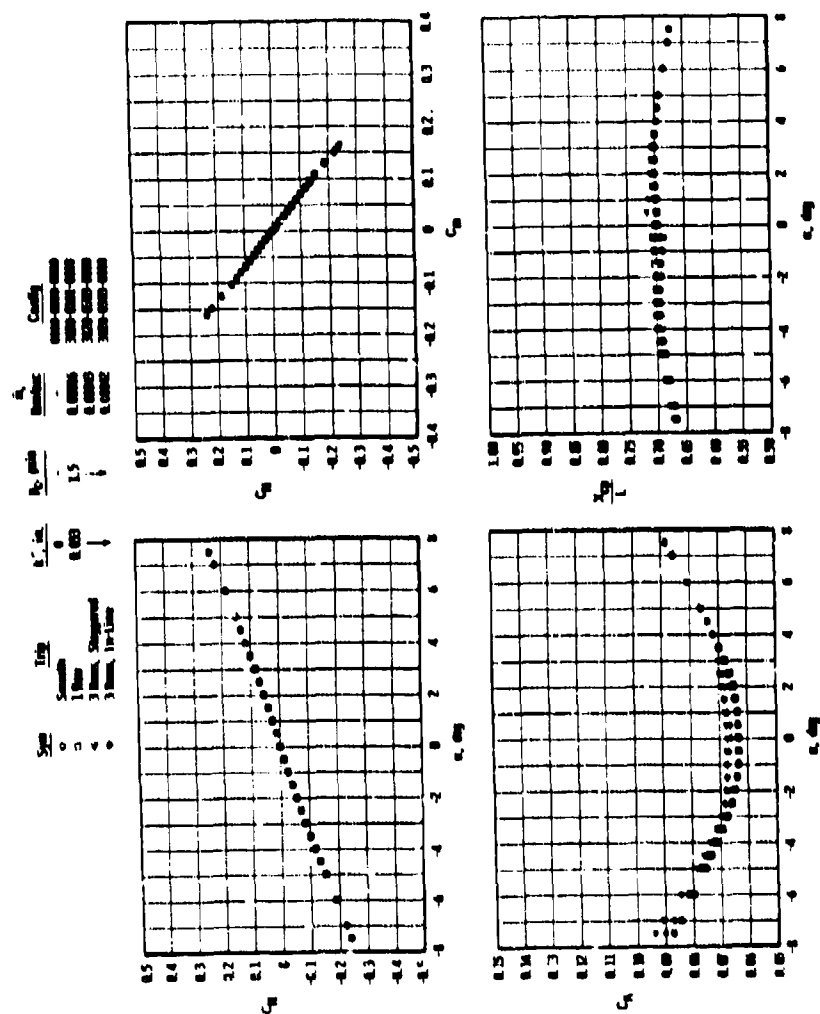


Figure 18. Effect of active trip configurations on the longitudinal stability and axial-force characteristics, $Re_{x,1} = 6.2 \times 10^6$.

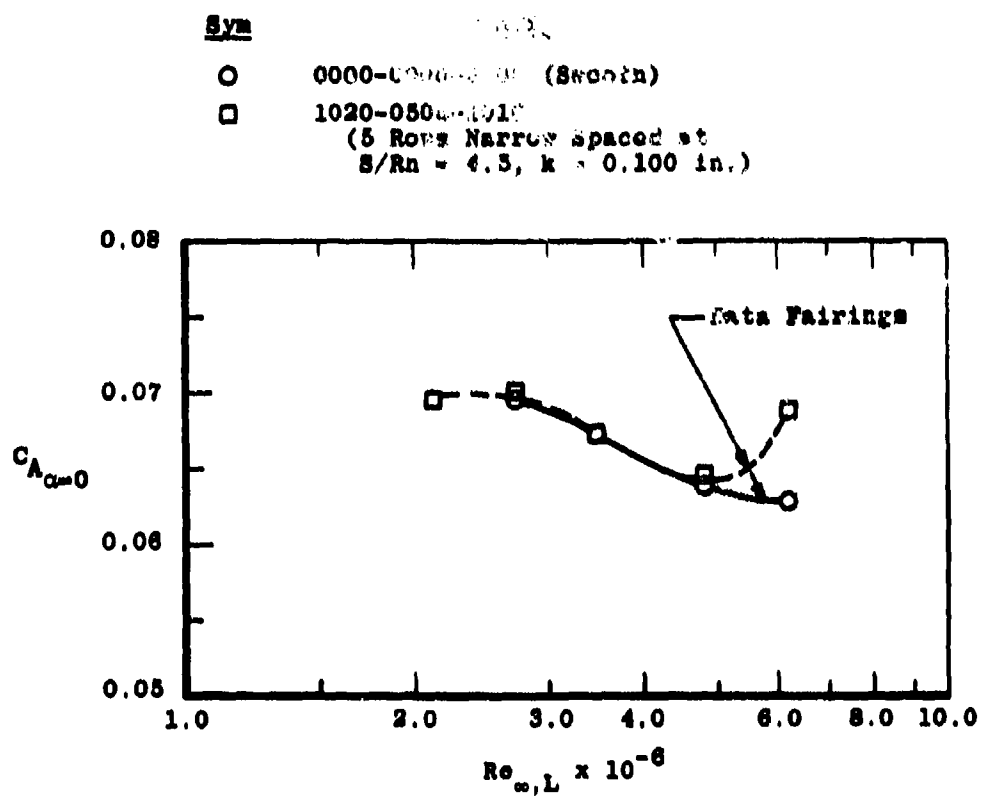


Figure 19. Effect of Reynolds number on axial force for a passive configuration (1020-0505-1010) at $\alpha = 0$.

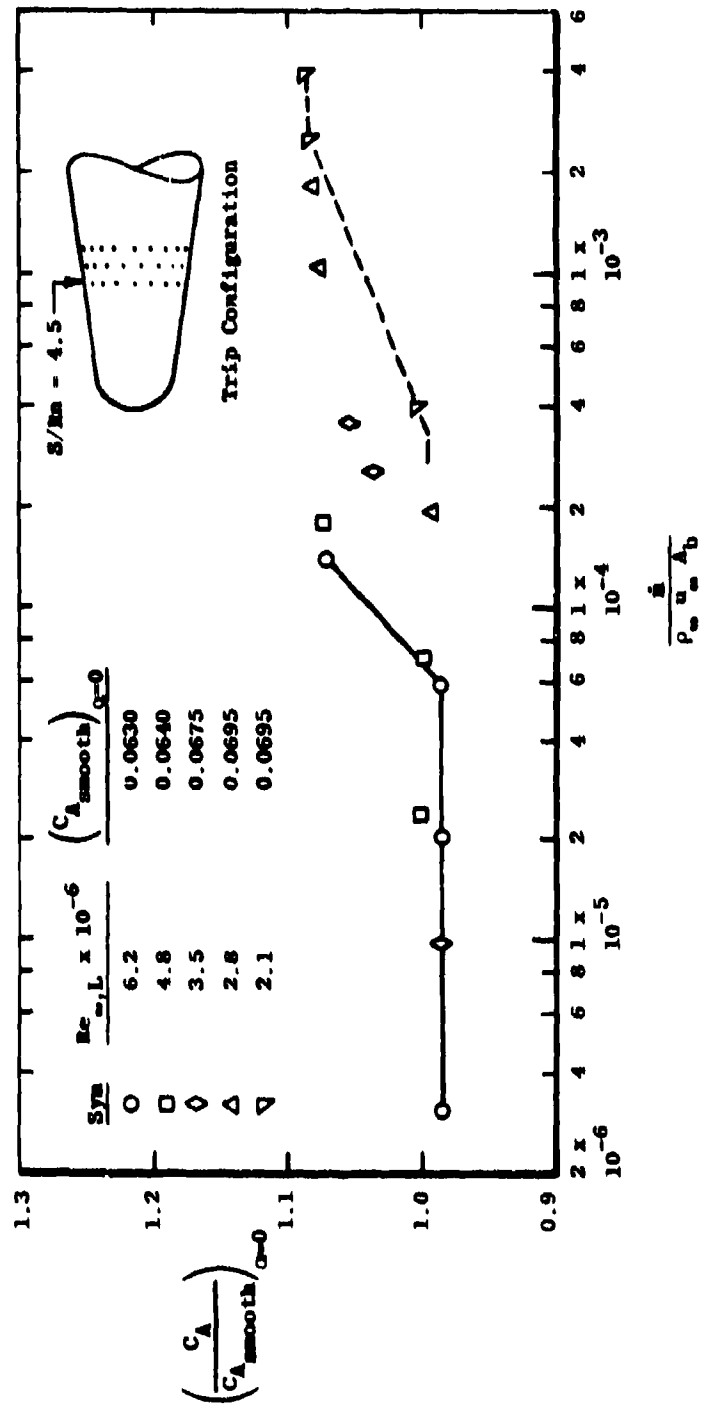


Figure 20. Effect of mass injection on axial force at $\alpha = 0$
for various Reynolds numbers (configuration
3120-0303-0000).

Table 1. Passive Trip Dimensions

CONFIGURATION			PART No.	S	Adiam' in.	Bdiam' in.	C, in.	D, in.	G, in.	Top Half			Bottom Half		
1	2	3								K ₁ ' in.	No. of Rows	No. of Trips	K ₂ ' in.	No. of Rows	No. of Trips
1040	0103	1005	1	4.5	2.122	2.784	2.515	0.650	0.800	0.100	1	5	0.050	3	5
1040	0103	1510	2			2.784	2.515		0.800	0.150	1	5	0.100	3	5
1040	0103	2015	3			2.784	2.515		0.800	0.200	1	5	0.150	3	5
1020	0103	1005	4			2.575	1.722		0.400	0.100	1	9	0.050	3	9
1020	0103	0505	4m							0.050	1	9	0.050	3	9
1020	0103	1510	5							0.100	1	9	0.100	3	9
1020	0103	1010	5m							0.100	1	9	0.100	3	9
1020	0103	2015	6							0.200	1	9	0.150	3	9
1020	0101	1010	6m							0.100	1	9	0.100	1	9
1020	0303	2020	7							0.200	3	9	0.200	3	9
1020	0303	1010	7m							0.100	3	9	0.100	3	9
2030	0103	1510	8	0.5	3.138	3.654	1.958	0.087	0.800	0.150	1	7	0.100	3	5
2030	0103	2015	9			3.654	1.958		0.800	0.200	1	7	0.150	3	5
2030	0103	3020	10			3.654	1.958		0.800	0.300	1	7	0.200	3	5
2015	0103	1510	11			3.445	1.765		0.400	0.150	1	13	0.100	3	11
2015	0103	2015	12			3.445	1.765		0.400	0.200	1	13	0.150	3	11
2015	0103	3020	13			3.445	1.765		0.400	0.300	1	13	0.200	3	11
1040	1010	0205	14	4.5	2.122	4.246	8.068	0.650	0.800	0.025	10	5	0.050	10	5
1040	1010	0710	15			4.246	8.068		0.800	0.075	10	5	0.100	10	5
1020	1010	0205	16			3.307	4.499		0.400	0.025	10	9	0.050	10	9
1020	1010	0710	17			3.307	4.499		0.400	0.075	10	9	0.100	10	9
1020	0505	0710	18			3.202	4.102		0.800	0.075	5	9	0.100	5	9
1020	1010	1010	19			3.307	4.499		0.400	0.100	10	9	0.100	10	9
1020	0505	1010	19m			3.307	4.499		0.400	0.100	5	9	0.100	5	9
1020	0303	1515	20			2.575	1.722		0.400	0.150	3	9	0.150	3	9
1020	1010	1515	21			3.307	4.499		0.400	0.150	10	9	0.150	10	9
2015	0303	2020	22	8.5	3.138	3.445	1.765	0.087	0.400	0.200	3	13	0.200	3	11
1040	0905	1515	33	4.5	2.122	4.246	8.068	0.650	0.800	0.150	9	9	0.150	9	9

Notes: 1. See Fig. 4 for definitions of Adiam', Bdiam', C, D, G, K₁' and K₂'.

2. Letter m denotes modified trip section.

3. Trip No. 7 was not tested.

Table 2. Heat-Transfer Test Summary
a. Passive Configurations

Configuration			$Re_{\infty, L}$ $\times 10^{-5}$	Angle of Attack, deg					Remarks
1	2	3		0	0.5	1.0	1.5	2.0	
0000 0000	0000 0000	0000 0000	2.8 2.8	x x		x x		x x	Smooth Body
1040 ↓	0103 ↓	1005 1510 2015	6.2 ↓	x x x					1 and 3 Rows, $S/R_n = 4.5$ Wide Spacing
1020 ↓	0103 ↓	1005 ↓ 1510 2015	1.5 2.1 2.8 3.5 4.1 4.8 5.5 6.2 ↓	x x x x x x x x x					1 and 3 Rows, $S/R_n = 4.5$ Narrow Spacing
2030 ↓	0103 ↓	1510 2015 3020	6.2 ↓	x x x					1 and 3 Rows, $S/R_n = 8.5$ Wide Spacing
2015 ↓	0103 ↓	1510 2015 3020	6.2 ↓	x x x					1 and 3 Rows, $S/R_n = 8.5$ Narrow Spacing
1040 1040	1010 1010	0205 0710	6.2 6.2	x x					10 Rows, $S/R_n = 4.5$ Wide Spacing
1020 ↓	1010 ↓	0205 0710	6.2 2.8 3.5 4.1 4.8 5.5 6.2 ↓	x x x x x x x x					10 Rows, $S/R_n = 4.5$ Narrow Spacing
1020	0505	0710	6.2	x					5 Rows, $S/R_n = 4.5$ Wide Axial Spacing Narrow Radial Spacing
1020 ↓	0303 ↓	1515 ↓	2.1 2.8 3.5 4.1 4.8 5.5 6.2 6.2 ↓	x x* x x x x x* x	x x x x x x x x	x x x x x x x x	x x x x x x x x	x x x x x x x x	3 Rows, $S/R_n = 4.5$ Narrow Spacing Symmetric Trips
2015		2020	6.2	x	x	x	x	x	$S/R_n = 8.5$
1040	0909	1515	6.2	x	x	x	x	x	9 Rows, $S/R_n = 4.5$ Wide Spacing Symmetric Trips
1020 ↓	1010 ↓	1010 1515	6.2 2.1 2.8 6.2 ↓	x x x x x	x x x x x	x x x x x	x x x x x	x x x x x	10 Rows, $S/R_n = 4.5$ Narrow Spacing Symmetric Trips

*Oil Flow Photographs at These Conditions

Table 2. Concluded
b. Active Configurations

Configuration			Re_n, L $\times 10^{-6}$	P_c , psia	Angle of Attack, deg					Remarks
1	2	3			0	0.5	1.0	1.5	2.0	
3040 ↓	0101 ↓	0000 ↓	6.2 ↓	1.5 14.6 32.7 58.2	x x x x	x x x x	x x x x	x x x x	x x x x	1 Row, $S/R_n = 4.5$ Wide Spacing
3020 ↓	0101 ↓	0000 ↓	2.1 ↓ 3.5 ↓ 4.8 ↓ 6.2 ↓	1.5 2.5 3.7 7.3 14.6 0.8 1.5 2.0 2.5 7.9 1.14 1.5 10.9 0 0.7 1.5 3.7 7.3 14.6 32.7 58.2 100	x x		x x		x x	1 Row, $S/R_n = 4.5$ Narrow Spacing
3040 ↓	0303 ↓	0000 ↓	6.2 ↓	1.5 3.6 7.0 14.6 32.7	x x x x x	x x x x x	x x x x x	x x x x x	x x x x x	3 Rows, $S/R_n = 4.5$ Wide Spacing
3020 ↓	0303 ↓	0000 ↓	2.1 ↓ 3.5 ↓ 4.8 ↓ 6.2 ↓	2.5 3.0 5.0 7.3 0.5 0.7 1.5 3.6 7.0 0.5 0.7 3.6 0.7 3.6 7.0	x x x x x x x x x x x x x x x x		x x x x x x x x x x x x x x x x		x x x x x x x x x x x x x x x x	3 Rows, $S/R_n = 4.5$ Narrow Spacing
3140 ↓	0303 ↓	0000 ↓	6.2 ↓	0.7 1.5 3.6 7.0	x x x x	x x x x	x x x x	x x x x	x x x x	Staggered Orifices 3 Rows, $S/R_n = 4.5$ Wide Spacing
3120 ↓	0303 ↓	0000 ↓		0.7 3.6 7.0	x x x	x x x	x x x	x x x	x x x	Staggered Orifices 3 Rows, $S/R_n = 4.5$ Narrow Spacing
4030 ↓	0101 ↓	0000 ↓		1.2 1.5 2.25 5.0 22.5 45.0	x x x x x x	x x x x x x	x x x x x x	x x x x x x	x x x x x x	1 Row, $S/R_n = 8.5$ Wide Spacing
4015 ↓	0101 ↓	0000 ↓		1.2 2.25 5.0	x x x	x x x	x x x	x x x	x x x	1 Row, $S/R_n = 8.5$ Narrow Spacing
3020 ↓	1010 ↓	0000 ↓		0.7 1.0 2.0	x x x	x x x	x x x	x x x	x x x	10 Rows, $S/R_n = 4.5$ Narrow Spacing

* Oil Flow Photographs at These Conditions

Table 3. Force Test Summary

CONFIGURATION			P _{C'} psia	Re _{u,L} x 10 ⁻⁶					REMARKS		
				6.2	4.8	3.5	2.8	2.1			
3020 ↓ 0101 ↓ 0303	↓ 0000	↓ 0000	0.70	x					Active Trips at S/R _n = 4.5	1 Row ↓ 3 ROWS 3 ROWS	
			1.50	x							
3120 ↓ 0000 ↓ 1020 ↓ A1020 ↓ 1020 ↓ 0303	↓ 0000	↓ 0000	3.00	x					Passive Trips at S/R _n = 4.5	3 Rows, Staggered	
			0.25	x							
			1.50	x							
			0.70	x							
			1.50	x							
			0.35	x							
			0.70	x							
			1.50	x							
			0.70	x							
			2.00	x							
			1.50	x							
			1.00	x							
			4.50	x							
			7.00	x							
			1.50	x							
			7.00	x							
10.00	x										
0000 ↓ 1020 ↓ A1020 ↓ 1020 ↓ 0303	↓ 0000	↓ 0000	0.70	x					Smooth Model 5 Rows, Symmetric Ablated Shape 1 and 3 Rows 1 Row, Symmetric 3 Rows, Symmetric 3 Rows, Symmetric		
			1.50	x							
			3.00	x							
			0.25	x							
			1.50	x							
			0.70	x							
			1.50	x							
			0.70	x							
			2.00	x							
			1.50	x							
			1.00	x							
			4.50	x							
			7.00	x							
			1.50	x							
			7.00	x							
			10.00	x							

NOMENCLATURE

A_b	Model aerodynamic reference area (base area), 78.54 in. ²
C_A	Model forebody axial-force coefficient, $C_A = C_{A_t} - C_{A_b}$
C_{A_b}	Model base axial-force coefficient, $C_{A_b} = -C_{p_b}$
C_{A_t}	Model total axial-force coefficient, $\frac{\text{total axial force}}{q_\infty A_b}$
C_m	Model pitching-moment coefficient, pitching moment/ $q_\infty A_b L$
C_{m_α}	Slope of pitching-moment curve, $\frac{dC_m}{d\alpha}$
C_N	Model normal-force coefficient, normal force/ $q_\infty A_b$
C_{N_α}	Slope of the normal-force curve, $\frac{dC_N}{d\alpha}$
C_{p_b}	Base pressure coefficient, $(p_b - p_\infty)/q_\infty$
d_s	Surface distance between trip elements (or orifices), center to center, in. (Constant in the axial direction; θ_s is constant in the radial direction, hence the value applies to the first row of trips only for radial spacing) $d_s = 0.400$ in. - Narrow Spacing $d_s = 0.800$ in. - Wide Spacing
H_o	Total enthalpy of air computed from the tunnel stilling chamber temperature (T_o), Btu/lbm

H_w Total enthalpy of air computed from the model wall temperature (T_w), Btu/lbm

k Passive trip element height above the model surface (see Fig. 4c)

k' Jet penetration height, distance from model surface to the normal shock wave in the jet plume (see Fig. 4d), in.

$$k' \approx 0.0129 \left(\frac{p_c}{p_{amb}} \right)^{1/2}$$

where p_{amb} = local ambient pressure at the jet exit, psia

$$p_{amb} = p_w \left[1 + 1.2 (M_e)^{1.5} (Re_{e,s})^{-0.25} \right]$$

p_w = local model wall pressure without mass injection (computed from inviscid theory), psia

M_e = local Mach number at edge of boundary layer without mass injection (computed from theory of Ref. 7)

$Re_{e,s}$ = local Reynolds number at edge of boundary layer without mass injection based on boundary-layer edge conditions at the jet location and the surface distance from the model nose

L Model aerodynamic reference length (total model length), 32.43 in.

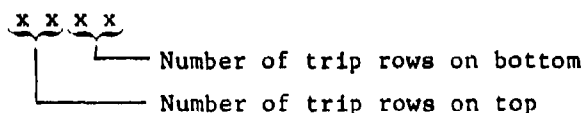
M_∞ Free-stream Mach number

\dot{m} Dry nitrogen mass injection rate for active trip configurations, lbm/sec

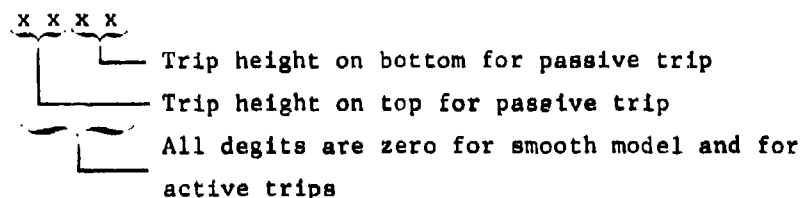
p_b Model base pressure, psia

P_c	Model plenum chamber pressure (active trip configurations only), psia
P_o	Tunnel stilling chamber pressure, psia
P_∞	Free-stream static pressure, psia
\dot{q}	Heat-transfer rate on the model surface, Btu/ft ² -sec
q_∞	Free-stream dynamic pressure, psia
R_b	Model base radius, 5.000 in.
$Re_{m,L}$	Reynolds number based on free-stream conditions and model reference length
R_n	Model nose radius, 0.833 in.
S	Model surface distance from the nose, in.
St	Stanton number, $\frac{\dot{q}}{\rho_\infty u_\infty (H_o - H_w)}$
St_{ref}	Reference Stanton number based on Fay-Riddell theory and the model nose radius of 0.833 in.
St_{turb}	Theoretical (Ref. 7) turbulent Stanton number for model at $\alpha = 0$
T_o	Tunnel stilling chamber temperature, °R
T_w	Model surface temperature, °R

(2)



(3)



Decimal point for trip height is .xx; if either set of digits is 02 or 07, add a 5 in the third decimal placing to obtain the trip height (0.025 or 0.075 in.)

TYPICAL CONFIGURATION:

1020-0103-1005 : Passive trip at $S/R_n = 4.5$ with a spacing between trips of $\theta_s = 20$ deg; one row of trips on top with a height of $k = 0.100$ in.; three rows of trips on the bottom with a height of $k = 0.050$ in.